PAPER • OPEN ACCESS

Linear and nonlinear excitation of TAE modes by external electromagnetic perturbations using ORB5

View the article online for updates and enhancements.

You may also like

Linear and nonlinear excitation of TAE modes by external electromagnetic perturbations using ORB5

Mohsen Sadr[1,*], **Alexey Mishchenko**[2], **Thomas Hayward-Schneider**[3], **Axel Koenies**[2], **Alberto Bottino**[3], **Alessandro Biancalani**[4,3], **Peter Donnel**[5], **Emmanuel Lanti**[1] **and Laurent Villard**[1]

[1] École Polytechnique Fédérale de Lausanne (EPFL), Swiss Plasma Center (SPC), Lausanne, CH-1015, Switzerland
[2] Max-Planck-Institut für Plasmaphysik, Greifswald, Germany
[3] Max-Planck-Institut für Plasmaphysik, Garching, Germany
[4] Léonard de Vinci Pôle Universitaire, Research Center, Paris la Défense, 92916, France
[5] CEA, IRFM, Saint-Paul-lez-Durance, F-13108, France

E-mail: msadr@mit.edu

CrossMark

Abstract

The excitation of toroidicity-induced Alfvén eigenmodes (TAEs) using prescribed external electromagnetic perturbations (hereafter 'antenna') acting on a confined toroidal plasma, as well as its nonlinear couplings to other modes in the system, is studied. The antenna is described by an electrostatic potential resembling the target TAE mode structure along with its corresponding parallel electromagnetic potential computed from Ohm's law. Numerically stable long-time linear simulations are achieved by integrating the antenna within the framework of a mixed representation and pullback scheme (Mishchenko *et al* 2019 *Comput. Phys. Commun.* **238** 194). By decomposing the plasma electromagnetic potential into symplectic and Hamiltonian parts and using Ohm's law, the destabilizing contribution of the potential gradient parallel to the magnetic field is cancelled in the equations of motion. Besides evaluating the frequencies and the growth/damping rates of excited modes compared to referenced TAEs, we study the interaction of antenna-driven modes with fast particles and indicate their margins of instability. Furthermore, we show the first nonlinear simulations in the presence of a TAE-like antenna exciting other TAE modes, as well as global Alfvén eigenmodes with different toroidal wave numbers from that of the antenna.

Keywords: linear, TAE, nonlinear, electromagnetic antenna, gyrokinetics, ORB5

(Some figures may appear in colour only in the online journal)

---

* Author to whom any correspondence should be addressed.

1. Introduction

Since toroidicity-induced Alfvén eigenmodes (TAEs) [5] can become destabilized when fast particles are included in the confined plasma [2, 6, 8, 22], analysis of the mode's structure for a given system of equations is of great interest. Ideally, from studying the mode behavior, one may predict and avoid the region of TAE instabilities that may be triggered in experiments. Although the growth rate and the frequency of the mode can be measured in simulations/ experiments when excited in the presence of fast particles, the estimation of the associated damping contributions can only be inferred indirectly, i.e. after subtracting the fast ion drive. When using an antenna, various modes can be resonantly excited and the damping rate can be directly measured from the plasma response, e.g. see the experiments performed in the Joint European Torus (JET) tokamak [7]. Moreover, eigenmodes that are overall stable can have their damping rate measured, whereas without antenna these modes do not show up.

TAE modes have been studied extensively in the literature through simulations of hybrid fluid-kinetic or gyrokinetic codes [1, 3, 11, 19, 23]. In particular, the linear gyrokinetic shear Alfvén physics (LIGKA) code [13–15] was developed in order to study the growth and damping of eigenmodes in the presence of energetic particles and a numerical antenna.

Motivated by previous works [18, 23], in this study we further develop an electrostatic and electromagnetic antenna [20] in the ORB5 code [12], i.e. a global electromagnetic gyrokinetic code using the particle-in-cell (PIC) approach in toroidal geometry, in order to excite the localized TAEs at a specific gap position in the vicinity of the rational $q = (|m| + 1/2)/|n|$ surface. Here, m and n are the poloidal and toroidal mode numbers, respectively, and q denotes the safety factor. The antenna is devised as an electrostatic potential and its electromagnetic counterpart is computed by solving Ohm's law. In order to allow simulations with large time step sizes, the self-consistent antenna field has been integrated into the equations of motion in the mixed-variable formulation as well as the celebrated pullback scheme of the δf method [16].

The content of this manuscript is organised as follows. In section 2, a short review of the mixed-variable formulation and the governing equations of ORB5, as well as the deployed solution algorithm, is provided. Next, the description of the antenna and its integration in the equations of motion is explained in section 3. Then in section 4, excitation of the TAE mode using the antenna is shown with several linear and nonlinear simulation results. Here, the frequency and damping rate of the mode in the linear setting is measured and compared to the results of fast particle simulations. Furthermore, for a plasma that is TAE-excited with an antenna, the margins of instability as a function of fast particle density have been studied. In nonlinear simulations using an $n = 6$ antenna, the excitation of an $n = 2$ TAE, as well as axisymmetric ($n = 0$) and

nonaxisymmetric ($n = 1$) global Alfvén eigenmodes (GAEs), is demonstrated. Concluding remarks and outlook are made in section 5.

2. Review: gyrokinetic model solved by ORB5

2.1. Mixed-variable collisionless kinetic equation solved by ORB5

In this section we review the governing equations that are solved with the global gyrokinetic PIC code ORB5 [12] in the framework of the pullback scheme [16]. First, the velocity distribution function is reduced to $f(\mathbf{R}, v_{||}, \mu; t)$ where $\mathbf{R}$ denotes the coordinates of the gyrocenter, $v_{||}$ is the component of velocity parallel to the magnetic field, and μ is the magnetic moment. By decomposing the reduced velocity distribution function associated with each species f_s into background control variate F_{0s} and the remaining δf_s, i.e. $f_s = F_{0s} + \delta f_s$, ORB5 solves the evolution of δf_s for each species following the gyrokinetic Vlasov–Maxwell system of equations, i.e.

$$\frac{\partial \delta f_s}{\partial t} + \dot{\mathbf{R}} \cdot \frac{\partial \delta f_s}{\partial \mathbf{R}}\bigg|_{v_{||}} + \dot{v}_{||} \frac{\partial \delta f_s}{\partial v_{||}} = -\dot{\mathbf{R}}^{(1)} \cdot \frac{\partial F_{0s}}{\partial \mathbf{R}}\bigg|_{\epsilon} - \dot{\epsilon}^{(1)} \frac{\partial F_{0s}}{\partial \epsilon},$$

(1)

using the method of characteristics. Here, $[\dot{\mathbf{R}}, \dot{v}_{||}]$ and $\epsilon = v_{||}^2/2 + \mu B$ are the gyrocenter trajectories and the energy of particle, respectively. The zeroth-order gyrocenter characteristics follow the common formulation

$$\dot{\mathbf{R}}^{(0)} = v_{||}\mathbf{b}^* + \frac{1}{qB_{||}^*}\mathbf{b} \times \mu\nabla B,$$

(2)

$$\text{and} \quad \dot{v}_{||}^{(0)} = -\frac{\mu}{m}\mathbf{b}^* \cdot \nabla B.$$

(3)

Here, the mixed-variable formulation is considered for the perturbation of trajectories which are computed from perturbed electrostatic potential ϕ, parallel electromagnetic potentials $A_{||}$ and magnetic field $\mathbf{B}$ in the linear field approximation (ignoring multiplication of perturbed fields), i.e.

$$\dot{\mathbf{R}}_{\text{plasma}}^{(1), \text{lin.fields}} = \frac{\mathbf{b}}{B_{||}^*} \times \nabla\langle\phi - v_{||}A_{||}^{(s)} - v_{||}A_{||}^{(h)}\rangle - \frac{q_s}{m_s}\langle A_{||}^{(h)}\rangle\mathbf{b}^*,$$

(4)

$$\dot{v}_{||, \text{plasma}}^{(1), \text{lin. fields}} = -\frac{q_s}{m_s}\left[\mathbf{b}^* \cdot \nabla\langle\phi - v_{||}A_{||}^{(h)}\rangle + \frac{\partial\langle A_{||}^{(s)}\rangle}{\partial t}\right] - \mu\frac{\mathbf{b} \times \nabla B}{B_{||}^*} \cdot \nabla\langle A_{||}^{(s)}\rangle,$$

(5)

and $\dot{\epsilon}_{\text{plasma}}^{(1), \text{ lin. fields}} = v_{||} \dot{v}_{||}^{(1), \text{ lin. fields}} + \mu \dot{\boldsymbol{R}}^{(1), \text{ lin. fields}} \cdot \nabla B$

$$= -\frac{q_s}{m_s} \left[m_s \mu \frac{\boldsymbol{b} \times \nabla B}{q_s B_{||}^*} + \frac{m_s v_{||}^2}{q_s B_{||}^*} \nabla \times \boldsymbol{b} \right] \cdot \nabla \langle \phi \rangle$$

$$+ \frac{q_s}{m_s} v_{||} \left[v_{||} \boldsymbol{b} + m_s \mu \frac{\boldsymbol{b} \times \nabla B}{q_s B_{||}^*} + \frac{m_s v_{||}^2}{q_s B_{||}^*} \nabla \times \boldsymbol{b} \right]$$

$$\cdot \nabla \langle A_{||}^{(h)} \rangle$$

$$+ \frac{q_s}{m_s} \mu B \left[\nabla \cdot \boldsymbol{b} - \frac{m_s v_{||}}{q B_{||}^*} \frac{\nabla \times \boldsymbol{B}}{B^2} \cdot \nabla B \right] \langle A_{||}^{(h)} \rangle, \tag{6}$$

where $\mu = v_\perp^2/(2B)$ is the magnetic moment, m_s is the mass of particle, q_s indicates the charge of the particle,

$$B_{||}^* = \boldsymbol{b} \cdot \nabla \boldsymbol{A}^*, \tag{7}$$

$$\boldsymbol{b}^* = \nabla \times \boldsymbol{A}^*/B_{||}^*, \tag{8}$$

$$\text{and} \quad \boldsymbol{A}^* = \boldsymbol{A} + \frac{m_s v_{||}}{q_s} \boldsymbol{b}. \tag{9}$$

In this formulation, $\boldsymbol{A}$ denotes the magnetic potential corresponding to the equilibrium magnetic field, i.e. $\boldsymbol{B} = \nabla \times \boldsymbol{A}$, and $\boldsymbol{b}$ indicates the unit vector $\boldsymbol{b} = \boldsymbol{B}/B$ where $B = |\boldsymbol{B}|$ is the magnitude of magnetic field at a given point in space. Furthermore, $A_{||}^{(h)}$ and $A_{||}^{(s)}$ denote the Hamiltonian and the symplectic parts of the perturbed magnetic potential, respectively, following the decomposition $A_{||} = A_{||}^{(s)} + A_{||}^{(h)}$. Moreover, the notation $\langle (.) \rangle$ indicates that the quantity of interest is gyro-averaged, i.e. $\langle (.) \rangle = \int (.)(\boldsymbol{R} + \boldsymbol{\rho}) d\alpha/(2\pi)$ where $\boldsymbol{\rho}$ is the gyroradius of the particle and α the gyro-phase.

In the fully nonlinear setting, the dominant nonlinear contribution originates from

$$\boldsymbol{B}^* = \boldsymbol{B} + \frac{m v_{||}}{q} \nabla \times \boldsymbol{b} + \nabla \langle A_{||}^{(s)} \rangle \times \boldsymbol{b} \tag{10}$$

$$\text{where} \quad \boldsymbol{b}^* = \frac{\boldsymbol{B}^*}{B_{||}^*} = \boldsymbol{b}_0^* + \frac{\nabla \langle A_{||}^{(s)} \rangle \times \boldsymbol{b}}{B_{||}^*} \tag{11}$$

$$\boldsymbol{b}_0^* \approx \boldsymbol{b} + \frac{m v_{||}}{q B_{||}^*} \nabla \times \boldsymbol{b}. \tag{12}$$

Hence, the outcome equations of motion in the mixed-variable formulation become nonlinear in terms of potentials, i.e.

$$\dot{\boldsymbol{R}}^{(1), \text{ nonlin. fields}} = \frac{\boldsymbol{b}}{B_{||}^*} \times \nabla \langle \phi - v_{||} A_{||}^{(s)} - v_{||} A_{||}^{(h)} \rangle$$

$$- \frac{q_s}{m_s} \langle A_{||}^{(h)} \rangle \left(\boldsymbol{b}_0^* + \frac{\nabla \langle A_{||}^{(s)} \rangle \times \boldsymbol{b}}{B_{||}^*} \right), \tag{13}$$

$$\dot{v}_{||}^{(1), \text{ nonlin. fields}} = -\frac{q_s}{m_s} \left[\left(\boldsymbol{b}_0^* + \frac{\nabla \langle A_{||}^{(s)} \rangle \times \boldsymbol{b}}{B_{||}^*} \right) \right.$$

$$\cdot \nabla \langle \phi - v_{||} A_{||}^{(h)} \rangle + \frac{\partial \langle A_{||}^{(s)} \rangle}{\partial t} \right]$$

$$- \mu \frac{\boldsymbol{b} \times \nabla B}{B_{||}^*} \cdot \nabla \langle A_{||}^{(s)} \rangle, \tag{14}$$

and $\dot{\epsilon}^{(1), \text{ nonlin. fields}} = v_{||} \dot{v}_{||}^{(1), \text{ nonlin. fields}} + \mu \dot{\boldsymbol{R}}^{(1), \text{ nonlin. fields}} \cdot \nabla B$

$$= -\frac{q_s}{m_s} \left[m_s \mu \frac{\boldsymbol{b} \times \nabla B}{q_s B_{||}^*} + \frac{m_s v_{||}^2}{q_s B_{||}^*} \nabla \times \boldsymbol{b} \right.$$

$$\left. + v_{||} \frac{\nabla \langle A_{||}^{(s)} \rangle \times \boldsymbol{b}}{B_{||}^*} \right] \cdot \nabla \langle \phi \rangle$$

$$+ \frac{q_s}{m_s} v_{||} \left[v_{||} \boldsymbol{b} + m_s \mu \frac{\boldsymbol{b} \times \nabla B}{q_s B_{||}^*} + \frac{m_s v_{||}^2}{q_s B_{||}^*} \nabla \times \boldsymbol{b} \right.$$

$$\left. + v_{||} \frac{\nabla \langle A_{||}^{(s)} \rangle \times \boldsymbol{b}}{B_{||}^*} \right] \cdot \nabla \langle A_{||}^{(h)} \rangle$$

$$+ \frac{q_s}{m_s} \mu B \left[\nabla \cdot \boldsymbol{b} - \frac{m_s v_{||}}{q B_{||}^*} \frac{\nabla \times \boldsymbol{B}}{B^2} \cdot \nabla B \right.$$

$$\left. - \frac{\nabla \langle A_{||}^{(s)} \rangle}{B_{||}^*} \cdot \frac{\boldsymbol{b} \times \nabla B}{B} \right] \langle A_{||}^{(h)} \rangle. \tag{15}$$

Note that the outcome nonlinearity for field potentials in the first order equations of motion, i.e. equations (13)–(15), enables mode-mode coupling. In order to have a self-contained system of equations, we need to introduce closures for the field quantities. The perturbed electrostatic potential ϕ is computed from the quasineutrality equation, here with the polarization density expressed in the long wavelength approximation

$$-\nabla \cdot \left[\left(\sum_{s=i,f} \frac{q_s^2 n_s}{T_s} \rho_s^2 \right) \nabla_\perp \phi \right] = \sum_{s=i,e,f} q_s n_{1,s}, \tag{16}$$

where $n_{1,s} = \int \delta f_s \delta(\boldsymbol{R} + \boldsymbol{\rho} - \boldsymbol{x}) d^6 Z$ indicates the perturbed gyrocenter density, $\rho_s = \sqrt{m_s T}/(q_s B)$ the thermal gyroradius, and $d^6 Z = B_{||}^* d\boldsymbol{R} \, dv_{||} \, d\mu \, d\alpha$ the phase-space infinitesimal volume. Once the electrostatic potential ϕ is computed, the symplectic part of parallel electromagnetic potential is obtained by solving Ohm's law

$$\frac{\partial}{\partial t} A_{||}^{(s)} + \boldsymbol{b} \cdot \nabla \phi = 0, \tag{17}$$

and the Hamiltonian part of electromagnetic potential $A_{||}^{(h)}$ from the mixed-variable parallel Ampere's law

---

Algorithm 1. The δf solution algorithm used in ORB5 within the linear pullback scheme

---

Initialize markers in phase space;
while $t < t_{\text{final}}$ **do**

    for $k = 1, \ldots, 4$ *step of Runge − Kutta scheme* **do**

        - Compute ϕ, $A_{||}^{(s)}$ and $A_{||}^{(h)}$ by solving equations (16)–(18);

        - Push particles according to zeroth-order equations of motion equations (2) and (3);

        - Apply boundary conditions;

    end

    - Update mixed-variable δf with $\delta f_s^{(m)} \leftarrow \delta f_s^{(m)} + \dfrac{q_s \langle A_{||}^{(h)} \rangle}{m_s} \dfrac{\partial F_{0s}}{\partial v_{||}}$;

    - Update $A_{||}$ decomposition, i.e, $A_{||}^{(s)} \leftarrow A_{||}^{(s)} + A_{||}^{(h)}$ and $A_{||}^{(h)} \leftarrow 0$;

    - $t = t + \Delta t$;

end

$$\left(\sum_{s=i,e,f} \frac{\beta_s}{\rho_s^2} - \nabla_\perp^2 \right) A_{||}^{(h)} = \mu_0 \sum_{s=i,e,f} j_{||,1s} + \nabla_\perp^2 A_{||}^{(s)}, \quad (18)$$

$$\text{and } j_{||,1s} = \int v_{||} \delta f_s \delta(\boldsymbol{R} + \boldsymbol{\rho} - \boldsymbol{x}) \mathrm{d}^6 Z \quad (19)$$

where $j_{||,1s}$ is the perturbed parallel gyrocenter current. The arbitrary splitting of the magnetic potential into parts and fixing the Hamiltonian part at the end of each time step allows us to contain the contribution of the skin term $\beta_e A_{||}^{(h)} / \rho_e^2$ which is associated with the cancellation problem, see [17] for details. While the symplectic part of $A_{||}$ is computed from Ohm's law, the nonideal contribution to the electromagnetic potential is included in this model by computing the Hamiltonian part of $A_{||}$ from Ampere's law.

2.2. Solution algorithm

The high dimensionality of the mixed distribution function is dealt with using the particle method. We discretize δf in the phase space with markers

$$\delta f_s^{(m)}(\boldsymbol{R}, v_{||}, \mu; t) = \sum_{i=1}^{N_p} \frac{1}{2\pi B_{||,i}^*} w_{s,i}(t) \delta(\boldsymbol{R} - \boldsymbol{R}_i) \delta(v_{||} - v_{||,i})$$
$$\times \delta(\mu - \mu_i) \quad (20)$$

where $\delta(.)$ indicates the Dirac delta function, N_p indicates the number of markers, and $w_{s,i}$ is the weight associated with the ith marker of species s. Having discretized the solution domain in the configuration space $\Omega \subset \mathbb{R}^3$ with an appropriately refined mesh, the densities in each computational cell can be estimated from the markers. Given the density field from particles, other required field quantities can be evaluated using the standard finite element method equipped with B-splines as the basis function to solve the quasi-neutrality equation, Ohm's law and Ampere's law, respectively. In particular,

$$\phi(s, \theta, \varphi, t) \approx \sum_{ljk} \hat{\phi}_{ljk}(t) \Lambda_{ljk}(s, \theta, \varphi), \quad (21)$$

$$A_{||}^{(s)}(s, \theta, \varphi, t) \approx \sum_{ljk} \hat{A}_{||,ljk}^{(s)}(t) \Lambda_{ljk}(s, \theta, \varphi), \quad (22)$$

$$\text{and} \quad A_{||}^{(h)}(s, \theta, \varphi, t) \approx \sum_{ljk} \hat{A}_{||,ljk}^{(h)}(t) \Lambda_{ljk}(s, \theta, \varphi), \quad (23)$$

where $\boldsymbol{\Lambda}$ is the tensor product of the usual B-splines λ in each direction, i.e. $\Lambda_{ljk}(s, \theta, \varphi) = \lambda_l(s) \lambda_k(\theta) \lambda_k(\varphi)$, and $\hat{(.)}$ indicates the projected coefficient. For detailed numerics of field computations, the reader is referred to [12].

Once electrostatic and electromagnetic potentials are computed, the particle representation of the distribution function is evolved by solving the zeroth-order evolution equations for the linear simulations, i.e. equations (2) and (3). In the nonlinear simulations, besides zeroth-order equations of motion, the first-order evolution equations of motion equations (4)–(6) or equations (13)–(15) are solved for linear field approximation and nonlinear fields, respectively. Note that in this study, the nonlinear simulations are performed, including the nonlinear field contributions. The outcome system of ordinary differential equations is solved using the standard fourth-order Runge–Kutta method. Although the Runge–Kutta time integration scheme that is deployed here is fourth-order accurate, it is neither conservative nor symplectic. This might affect very long simulations, but for all cases under study in this paper we do not observe any deleterious effect.

The pullback scheme enters the solution algorithm by updating symplectic and Hamiltonian parts of $A_{||}$ as well as updating the symplectic part of the distribution function at the end of each iteration. This separation combined with the control variate nature of the δf method allows for long and stable simulations. Short explanations of the pullback scheme for both linear and nonlinear settings are provided in algorithms 1 and 2, respectively [16].

Algorithm 2. The δf solution algorithm used in ORB5 within the nonlinear pullback scheme.

Initialize markers in the phase space;
while $t < t_{\text{final}}$ **do**

    for $k = 1, \ldots, 4$ *step of Runge–Kutta scheme* **do**

        - Compute ϕ, $A_{||}^{(s)}$ and $A_{||}^{(h)}$ by solving equations (16)–(18);
        - Push particles according to the zeroth and first-order equations of motion equations (2) and (3) and equations (13)–(15);
        - Apply boundary conditions;
    end

    - Transform the phase-space coordinates keeping the particle weights, i.e. $v_{||}^{(m),\,\text{new}} \leftarrow v_{||}^{(m),\,\text{old}} - \frac{q_s}{m_s} \langle A_{||}^{(h)} \rangle$ and $f_{1s}^{(m)}(v_{||}^{(m),\text{new}}) \leftarrow f_{1s}^{(m)}(v_{||}^{(m),\text{old}})$;
    - Update $A_{||}$ decomposition, i.e, $A_{||}^{(s)} \leftarrow A_{||}^{(s)} + A_{||}^{(h)}$ and $A_{||}^{(h)} \leftarrow 0$;
    - $t = t + \Delta t$;

end

---

3. Antenna

The idea is to excite the eigenmode of interest using an external targeted force/drift in the equations of motion [4]. This can be achieved by describing the external force as the gradient of a potential which resembles the target mode structure and frequency. Having described such an external potential, one can extend the plasma's equations of motion including the antenna field by substituting ϕ with $\phi_{\text{ant}} + \phi_{\text{plasma}}$ as well as $A_{||}$ with $A_{||,\text{ant}} + A_{||,\text{plasma}}$.

3.1. Devising an electrostatic potential for antenna

Consider the antenna as an electrostatic potential described by

$$
\begin{aligned}
\phi_{\text{ant}}(s,\theta,\varphi;t) &= \text{Re}\left[\sum_{I\in\mathcal{T}} h_I(s)A_I e^{\hat{i}(I_1\,\theta + I_2\,\varphi + \Phi_I)}(c_1 + c_2 e^{\hat{i}w_{\text{ant}}t})\right] \\
&= (c_1 + c_2\,\cos(\omega_{\text{ant}}t)) \\
&\quad \times \underbrace{\left(\sum_{I\in\mathcal{T}} h_I(s)A_I\cos\left(I_1\,\theta + I_2\,\varphi + \Phi_I\right)\right)}_{S_{\text{ant},1}(s,\theta,\varphi):=} \\
&\quad + c_2\,\sin(\omega_{\text{ant}}t) \\
&\quad \underbrace{\left(\sum_{I\in\mathcal{T}} h_I(s)A_I\cos\left(I_1\,\theta + I_2\,\varphi + \Phi_I + \frac{\pi}{2}\right)\right)}_{S_{\text{ant},2}(s,\theta,\varphi):=},
\end{aligned}
\tag{24}
$$

where the set $\mathcal{T} = \{(m_1,n_1),\ldots\}$ contains all the targeted mode number pairs, A_I denotes the mode coefficient for the *I*th mode, Φ_I is its phase offsets, $c_1, c_2 \in \mathbb{R}$ are the coefficients of the static and oscillating components, respectively, $\hat{i}$ is the imaginary number, and ω_{ant} is the antenna's frequency. The radial profile $h(s)$ is chosen as an input. Since field properties

in ORB5 are stored in the B-spline basis function, we need to project ϕ_{ant} to $\mathbf{\Lambda}$. The presented decomposition of potential into time dependent and independent parts in equation (24) saves computational time since the projections of the time independent parts of ϕ_{ant}, i.e. S_1 and S_2, can be computed at the beginning of the simulation.

Following ORB5's approach of the evaluation of field properties at the particle positions, the antenna's potential described in equation (24) needs to be projected into B-spline basis function. In particular, the time-independent parts of the antenna's potential in equation (24), i.e. $S_{\text{ant}} = S_{\text{ant},1}(s,\theta,\phi)$ and $S_{\text{ant},2}(s,\theta,\phi)$, shall be projected

$$
S_{\text{ant}} = \sum_{ijk} \hat{S}_{\text{ant},ijk}\Lambda_{ijk}(s,\theta,\varphi) \tag{25}
$$

$$
\text{where}\quad \Lambda_{ijk}(s,\theta,\phi) = \lambda_i(s)\lambda_j(\theta)\lambda_k(\phi). \tag{26}
$$

Here, λ indicates 1D B-spline polynomials, $\hat{S}_{\text{ant}}$ indicates the projected coefficients which can be obtained using the weak form

$$
\int S_{\text{ant}}\psi\,\mathrm{d}V = \int \hat{S}_{\text{ant}}\psi\,\mathrm{d}V\,\forall\psi; \tag{27}
$$

where B-spline basis functions are taken for the test function ψ. The projected coefficients are obtained by solving the linear system of equations

$$
\sum_{i'j'k'} M_{ijk\,i'j'k'}\hat{S}_{\text{ant},i'j'k'}\,\mathrm{d}V = \underbrace{\int S_{\text{ant}}\Lambda_{ijk}\mathrm{d}V}_{b_{\text{ant},imn}}, \tag{28}
$$

where $M_{ijk\,i'j'k'} = \int J(s,\theta)\Lambda_{ijk}(s,\theta,\varphi)\Lambda_{i'j'k'}(s,\theta,\varphi)\mathrm{d}s\mathrm{d}\theta\mathrm{d}\varphi$,

$$
\tag{29}
$$

and $\mathrm{d}V = \mathrm{d}^3 \boldsymbol{x}$ is the infinitesimal volume in configuration space. This system of equations is solved in discrete Fourier space

$$\sum_{i'=1}^{N_s+p} \sum_{n'=n_{\min}}^{n_{\max}} \sum_{m'=-n'q_{i'}-\Delta m}^{-n'q_{i'}+\Delta m} \tilde{M}_{ijk\,i'j'k'} \tilde{\tilde{S}}_{\mathrm{ant},i'm'n'} = \tilde{b}_{\mathrm{ant},imn} \quad (30)$$

where the integrals are computed numerically using the Gaussian quadrature rule [20].

3.2. Electromagnetic antenna

Motivated by the pullback scheme and mitigation cancellation, instead of considering an arbitrary electromagnetic potential for the antenna, we impose $A_{\mathrm{ant},||} = A_{\mathrm{ant},||}^{(s)} + A_{\mathrm{ant},||}^{(h)}$ where the symplectic part follows Ohm's law

$$\frac{\partial}{\partial t} A_{\mathrm{ant},||}^{(s)} + \boldsymbol{b} \cdot \nabla \phi_{\mathrm{ant}} = 0, \quad (31)$$

and the Hamiltonian part $A_{\mathrm{ant},||}^{(h)} = 0$. Here, the ϕ_{ant} is an arbitrary electrostatic potential described according to the target mode of interest, as described in section 3.1.

3.3. Integrating electrostatic antenna in the equations of motion

The equations of motion for an electrostatic antenna described can be naturally developed by substituting $\phi + \phi_{\mathrm{ant}}$ instead of ϕ in the plasma's equation of motion equations (4)–(6) leading to

$$\dot{\boldsymbol{R}}^{(1),\,\mathrm{lin.\,fields}} = \dot{\boldsymbol{R}}_{\mathrm{plasma}}^{(1),\,\mathrm{lin.\,fields}} + \frac{\boldsymbol{b}}{B_{||}^*} \times \nabla \langle \phi_{\mathrm{ant}} \rangle, \quad (32)$$

$$\dot{v}_{||}^{(1),\,\mathrm{lin.\,fields}} = \dot{v}_{||,\mathrm{plasma}}^{(1),\,\mathrm{lin.\,fields}} - \frac{q_s}{m_s} \boldsymbol{b}^* \cdot \nabla \langle \phi_{\mathrm{ant}} \rangle, \quad (33)$$

$$\dot{\epsilon}^{(1),\,\mathrm{lin.\,fields}} = \dot{\epsilon}_{\mathrm{plasma}}^{(1),\,\mathrm{lin.\,fields}} - \frac{q_s}{m_s}$$
$$\times \left[\frac{v_{||}\boldsymbol{B}}{B_{||}^*} + m_s \mu \frac{\boldsymbol{b} \times \nabla B}{q_s B_{||}^*} + \frac{m_s v_{||}^2}{q_s B_{||}^*} \nabla \times \boldsymbol{b} \right] \cdot \nabla \langle \phi_{\mathrm{ant}} \rangle. \quad (34)$$

for the pullback scheme linearized with respect to the field perturbations, and

$$\dot{\boldsymbol{R}}^{(1),\,\mathrm{nonlin.\,fields}} = \dot{\boldsymbol{R}}_{\mathrm{plasma}}^{(1),\,\mathrm{nonlin.\,fields}} + \frac{\boldsymbol{b}}{B_{||}^*} \times \nabla \langle \phi_{\mathrm{ant}} \rangle, \quad (35)$$

$$\dot{v}_{||}^{(1),\,\mathrm{nonlin.\,fields}} = \dot{v}_{||,\,\mathrm{plasma}}^{(1),\,\mathrm{nonlin.\,fields}} - \frac{q_s}{m_s} \boldsymbol{b}^* \cdot \nabla \langle \phi_{\mathrm{ant}} \rangle, \quad (36)$$

$$\dot{\epsilon}^{(1),\,\mathrm{nonlin.\,fields}} = \dot{\epsilon}_{\mathrm{plasma}}^{(1),\,\mathrm{nonlin.\,fields}}$$
$$- \frac{q_s}{m_s} \left[\frac{v_{||}\boldsymbol{B}}{B_{||}^*} + m_s \mu \frac{\boldsymbol{b} \times \nabla B}{q_s B_{||}^*} + \frac{m_s v_{||}^2}{q_s B_{||}^*} \nabla \times \boldsymbol{b} \right.$$
$$\left. + v_{||} \frac{\nabla \langle A_{||}^{(s)} \rangle \times \boldsymbol{b}}{B_{||}^*} \right] \cdot \nabla \langle \phi_{\mathrm{ant}} \rangle. \quad (37)$$

for the nonlinear pullback scheme. Here, the subscript $(.)_{\mathrm{plasma}}$ indicates the plasma contribution to the equations of motion and energy, i.e. equations (4)–(6) for linear field approximation and equations (13)–(15) for nonlinear formulation.

It can be of interest to perform numerical simulations in the presence of the antenna where the plasma response is linearized. For consistency, one needs to use the linearized pullback scheme, equations (32)–(34), where the terms corresponding to the plasma response in the equations of motion, i.e. $\dot{\boldsymbol{R}}_{\mathrm{plasma}}^{(1)\,\mathrm{lin.fields}}$ and $\dot{v}_{\mathrm{plasma}}^{(1)\,\mathrm{lin.fields}}$ in the left hand side of kinetic equation (1), are set to zero.

Note that the appearance of $v_{||}\boldsymbol{B} \cdot \nabla \langle \phi_{\mathrm{ant}} \rangle$ causes a numerical challenge as it pushes particles further in the parallel direction. Motivated by the treatment of such terms in the pullback scheme, next we consider equations of motion for the electromagnetic antenna.

3.4. Integrating electromagnetic antenna in the equations of motion

In order to obtain long and stable simulations of TAE excitation with the antenna, we use Ohm's law to introduce the electromagnetic antenna in the equations of motion and mimic the treatment of the cancellation problem in the mixed-variable formulation, see section 2.2. We derive equations of motion corresponding to the antenna's field by natural extension of the plasma's equations of motion where we substitute $\phi + \phi_{\mathrm{ant}}$ instead of the plasma's electrostatic potential ϕ and $A_{||}^{(s)} + A_{||,\mathrm{ant}}^{(s)}$ instead of $A_{||}^{(s)}$. Hence, one obtains for the linear field approximation

$$\dot{\boldsymbol{R}}^{(1),\,\mathrm{lin.\,fields}} = \dot{\boldsymbol{R}}_{\mathrm{plasma}}^{(1),\,\mathrm{lin.\,fields}} + \frac{\boldsymbol{b}}{B_{||}^*} \times \nabla \langle \phi_{\mathrm{ant}} \rangle - \frac{\boldsymbol{b}}{B_{||}^*}$$
$$\times \nabla \langle v_{||} A_{||,\mathrm{ant}}^{(s)} \rangle, \quad (38)$$

$$\dot{v}_{||}^{(1),\,\mathrm{lin.\,fields}} = \dot{v}_{||,\mathrm{plasma}}^{(1),\,\mathrm{lin.\,fields}} - \frac{q_s}{m_s} (\boldsymbol{b}^* - \boldsymbol{b}) \cdot \nabla \langle \phi_{\mathrm{ant}} \rangle$$
$$- \frac{\mu}{B_{||}^*} \boldsymbol{b} \times \nabla B \cdot \nabla \langle A_{||,\mathrm{ant}}^{(s)} \rangle, \quad (39)$$

and $\dot{\epsilon}^{(1),\,\mathrm{lin.\,fields}} = \dot{\epsilon}_{\mathrm{plasma}}^{(1),\,\mathrm{lin.\,fields}} - \frac{q_s}{m_s}$
$$\times \left[m_s \mu \frac{\boldsymbol{b} \times \nabla B}{q_s B_{||}^*} + \frac{m_s v_{||}^2}{q_s B_{||}^*} \nabla \times \boldsymbol{b} \right] \cdot \nabla \langle \phi_{\mathrm{ant}} \rangle. \quad (40)$$
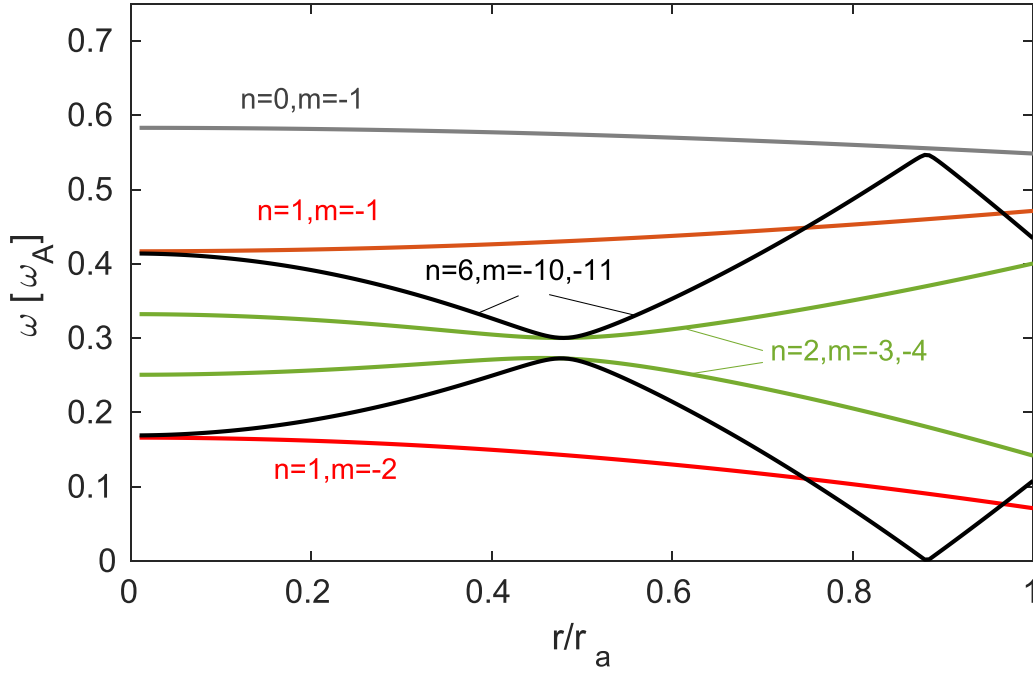
Figure 1. Alfvén continua of ITPA test case for $n = 0, 1, 2$ and six toroidal mode numbers.

Here, Ohm's law on the antenna equation (31) was deployed to cancel out destabilizing terms, i.e. cancellation of $\partial A_{||,\text{ant}}^{(s)}/\partial t$ terms. More precisely, we found that this procedure allowed us to preserve the benefits provided by the pullback scheme, resulting in the possibility of performing numerically stable simulations with large time steps. In the case of nonlinear mixed variable formulation, one obtains

$$\dot{\boldsymbol{R}}^{(1),\text{ nonlin. fields}} = \dot{\boldsymbol{R}}_{\text{plasma}}^{(1),\text{ nonlin. fields}} + \frac{\boldsymbol{b}}{B_{||}^*} \times \nabla \langle \phi_{\text{ant}} - v_{||} A_{||,\text{ant}}^{(s)} \rangle$$

$$- \frac{q}{m} \langle A_{||}^{(h)} \rangle \frac{\nabla \langle A_{||,\text{ant}}^{(s)} \rangle \times \boldsymbol{b}}{B_{||}^*}, \qquad (41)$$

$$\dot{v}_{||}^{(1),\text{ nonlin. fields}} = \dot{v}_{||,\text{ plasma}}^{(1),\text{ nonlin. fields}}$$

$$- \left(\frac{v_{||}}{B_{||}^*} \nabla \times \boldsymbol{b} + \frac{q}{m} \frac{\nabla \langle A_{||}^{(s)} \rangle \times \boldsymbol{b}}{B_{||}^*} \right) \cdot \nabla \langle \phi_{\text{ant}} \rangle$$

$$- \frac{q}{m} \frac{\nabla \langle A_{||,\text{ant}}^{(s)} \rangle \times \boldsymbol{b}}{B_{||}^*} \cdot \nabla \langle \phi - v_{||} A_{||}^{(h)} \rangle$$

$$- \frac{q}{m} \frac{\nabla \langle A_{||,\text{ant}}^{(s)} \rangle \times \boldsymbol{b}}{B_{||}^*} \cdot \nabla \langle \phi_{\text{ant}} \rangle$$

$$- \mu \frac{\boldsymbol{b} \times \nabla B}{B_{||}^*} \cdot \nabla \left\langle A_{||,\text{ant}}^{(s)} \right\rangle, \qquad (42)$$

and $\dot{\epsilon}^{(1),\text{ nonlin. fields}}$

$$= \dot{\epsilon}_{\text{plasma}}^{(1),\text{ nonlin. fields}} - \frac{q_s}{m_s} \left[\frac{v_{||}\boldsymbol{B}}{B_{||}^*} + m_s\mu \frac{\boldsymbol{b} \times \nabla B}{q_s B_{||}^*} + \frac{m_s v_{||}^2}{q_s B_{||}^*} \nabla \times \boldsymbol{b} \right.$$

$$\left. + v_{||} \frac{\nabla \langle A_{||}^{(s)} \rangle \times \boldsymbol{b}}{B_{||}^*} \right] \cdot \nabla \langle \phi_{\text{ant}} \rangle$$

$$- \frac{q_s}{m_s} \left[v_{||} \frac{\nabla \langle A_{||,\text{ant}}^{(s)} \rangle \times \boldsymbol{b}}{B_{||}^*} \right] \cdot \nabla \langle \phi \rangle - \frac{q_s}{m_s} \left[v_{||} \frac{\nabla \langle A_{||,\text{ant}}^{(s)} \rangle \times \boldsymbol{b}}{B_{||}^*} \right] \cdot \nabla \langle \phi_{\text{ant}} \rangle$$

$$+ \frac{q_s}{m_s} v_{||} \left[v_{||} \frac{\nabla \langle A_{||,\text{ant}}^{(s)} \rangle \times \boldsymbol{b}}{B_{||}^*} \right] \cdot \nabla \langle A_{||}^{(h)} \rangle$$

$$- \frac{q_s}{m_s} \mu B \left[\frac{\nabla \langle A_{||,\text{ant}}^{(s)} \rangle}{B_{||}^*} \cdot \frac{\boldsymbol{b} \times \nabla B}{B} \right] \langle A_{||}^{(h)} \rangle. \qquad (43)$$

Often, one might be interested in exciting a mode using an electromagnetic antenna with linearized plasma response. In that case, it is necessary to use the linearized pullback scheme, equations (38)–(40), in which the plasma response terms in the equations of motion, i.e. $\dot{\boldsymbol{R}}_{\text{plasma}}^{(1)\text{ lin.fields}}$ and $\dot{v}_{\text{plasma}}^{(1)\text{ lin.fields}}$ in the left hand side of kinetic equation (1), are ignored.

4. Results

In this section, we deploy the described antenna in ORB5 in order to excite TAE modes in the linear setting, i.e. section 4.2, where we measure the frequency and the damping rate, i.e. in section 4.2.2, as well as study the margins of instability in the presence of fast particles, i.e. in section 4.2.3. Then, nonlinear
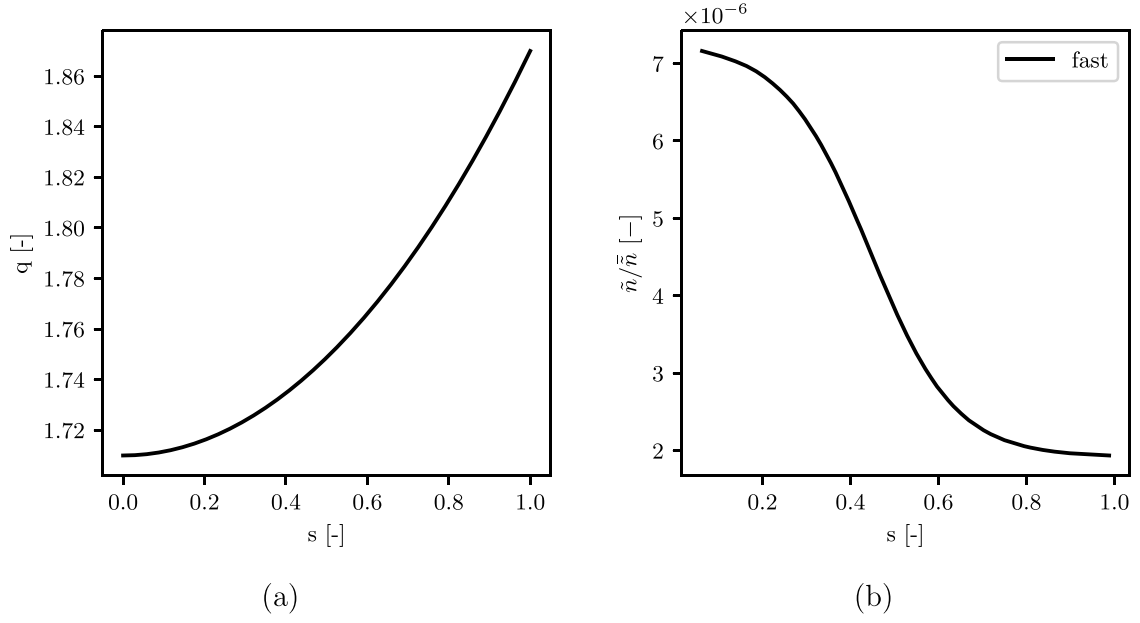
(a)

(b)

Figure 2. The radial profile of (a) safety factor q and (b) the normalized number density of fast particles in the ITPA test case.
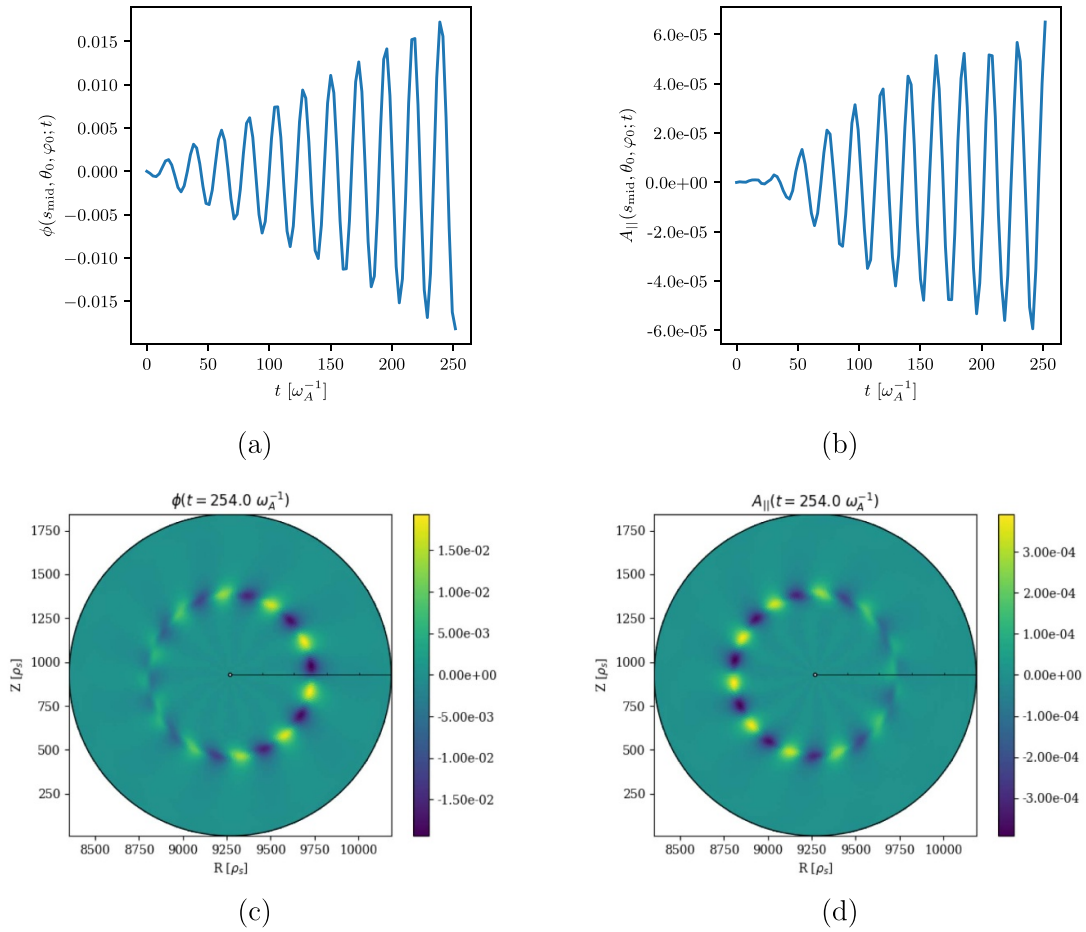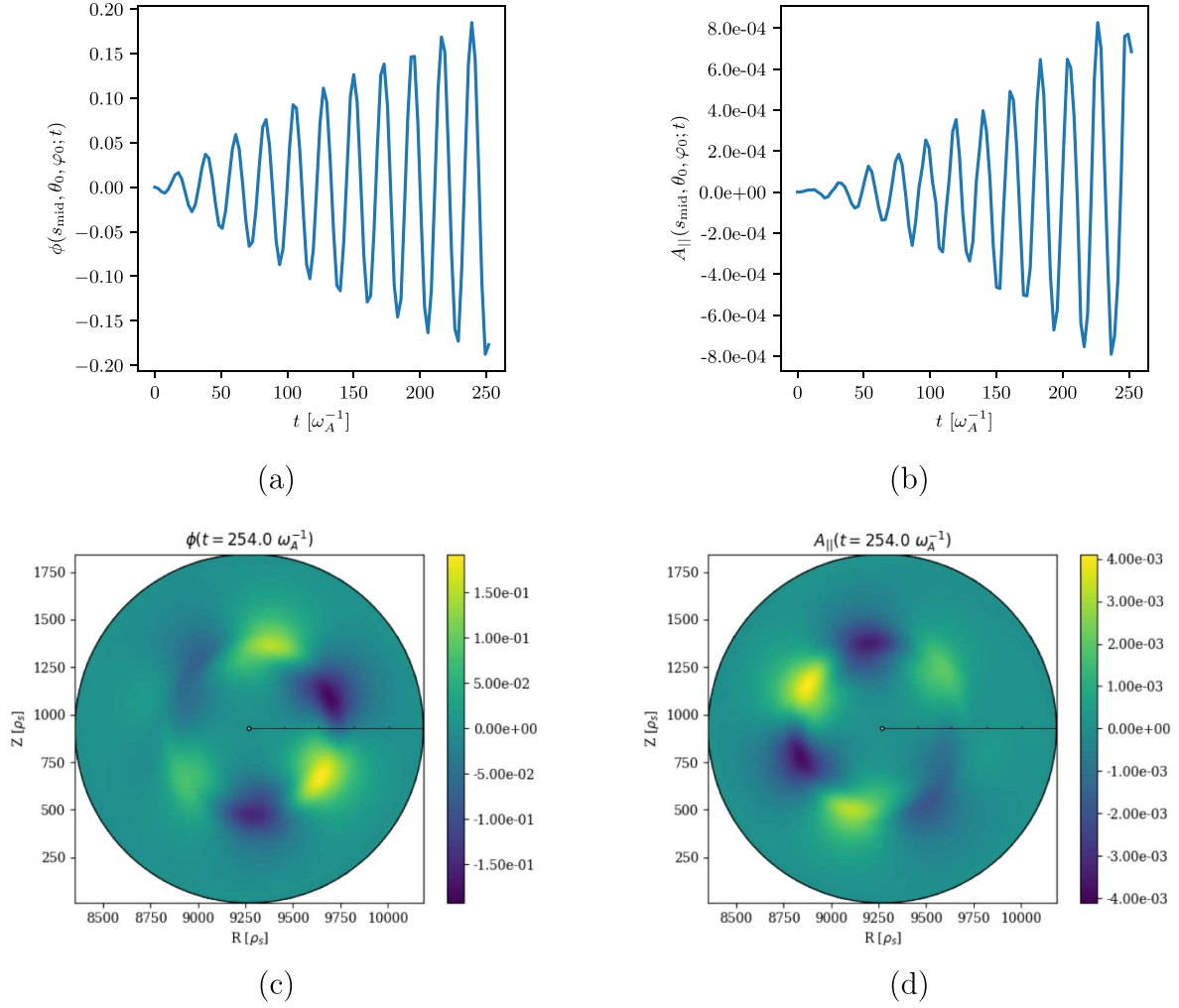

(a)

(b)

(c)

(d)

Figure 3. Linear growth of (a) electrostatic and (b) electromagnetic plasma's potentials evaluated at the mid point $s = 1/2$ on the axis $\theta_0 = \varphi_0 = 0$ for the $n = 6$ TAE mode excitation with an electromagnetic antenna. The potentials for the given toroidal angle is depicted in (c) and (d).

(a)

(b)

(c)

(d)

Figure 4. Linear growth of (a) electrostatic and (b) electromagnetic plasma's potentials evaluated at the mid point $s = 1/2$ on the axis $\theta_0 = \varphi_0 = 0$ for the $n = 2$ TAE mode excitation with an electromagnetic antenna. The potentials for a given toroidal angle are depicted in (c) and (d).

simulation results of exciting various TAE and GAE modes using the antenna are presented in section 4.3.

4.1. Simulation setting

Here, we consider the international cross-code reference test case 'ITPA-TAE' [11], where the toroidal Alfvén eigenmode with the toroidal mode number $n = 6$ and the dominant poloidal mode numbers $m = -10$ and $m = -11$ are considered in the linear regime. Further investigations indicated that there is another TAE gap mode in this test case with $n = 2$ and $m = -4, -3$, see figure 1 for the Alfvén continua of the ITPA test case. These modes are studied in tokamak-size geometry with the minor radius $r_a = 1$ m, major radius $R_0 = 10$ m, magnetic field on axis $B_0 = 3$ T, and the safety factor profile $q(r) = 1.71 + 0.16(r/r_a)^2$, where r is the geometric radial coordinate. We consider flat background plasma profiles with the ion number density $n_i = 2 \times 10^{19}$ m^{-3}, a mass ratio of $m_i/m_e = 200$,

ion and electron temperatures of $T_i = T_e = 1$ keV which correspond to $\beta_{bulk} = 2\mu_0(n_i T_i + n_e T_e)/B_0^2 \approx 0.18\%$. Here, μ_0 is the permeability of the vacuum and n_s is the number density of species s which is related to the mass density ρ_s via $\rho_s = n_s m_s$. In some cases, we deploy fast particles with a Maxwellian distribution in velocity space and a flat radial profile of temperature $T_f = 400$ keV and a number density with the profile

$$\tilde{n} = n_{0f} \exp\left(-w\kappa_n \tanh\left(\frac{s-a}{w}\right)\right) \quad \text{and} \quad n_f = \tilde{n}/\bar{\tilde{n}} \quad (44)$$

where $\bar{(.)}$ indicates the annular averaged value, and the values for the parameters $w = 0.2$, $\kappa_n = 3.333$, $a = 0.5$, and $n_{0f} = 0.0031$ are taken from [11]. See figure 2 for the profiles of initial density of fast particles and the safety factor in the radial direction $s = \sqrt{\psi/\psi_{edge}}$. Here, ψ is the poloidal magnetic flux and ψ_{edge} denotes its value at the radial edge.

Following a convergence study for the linear simulations, the simulation results reported here are obtained using
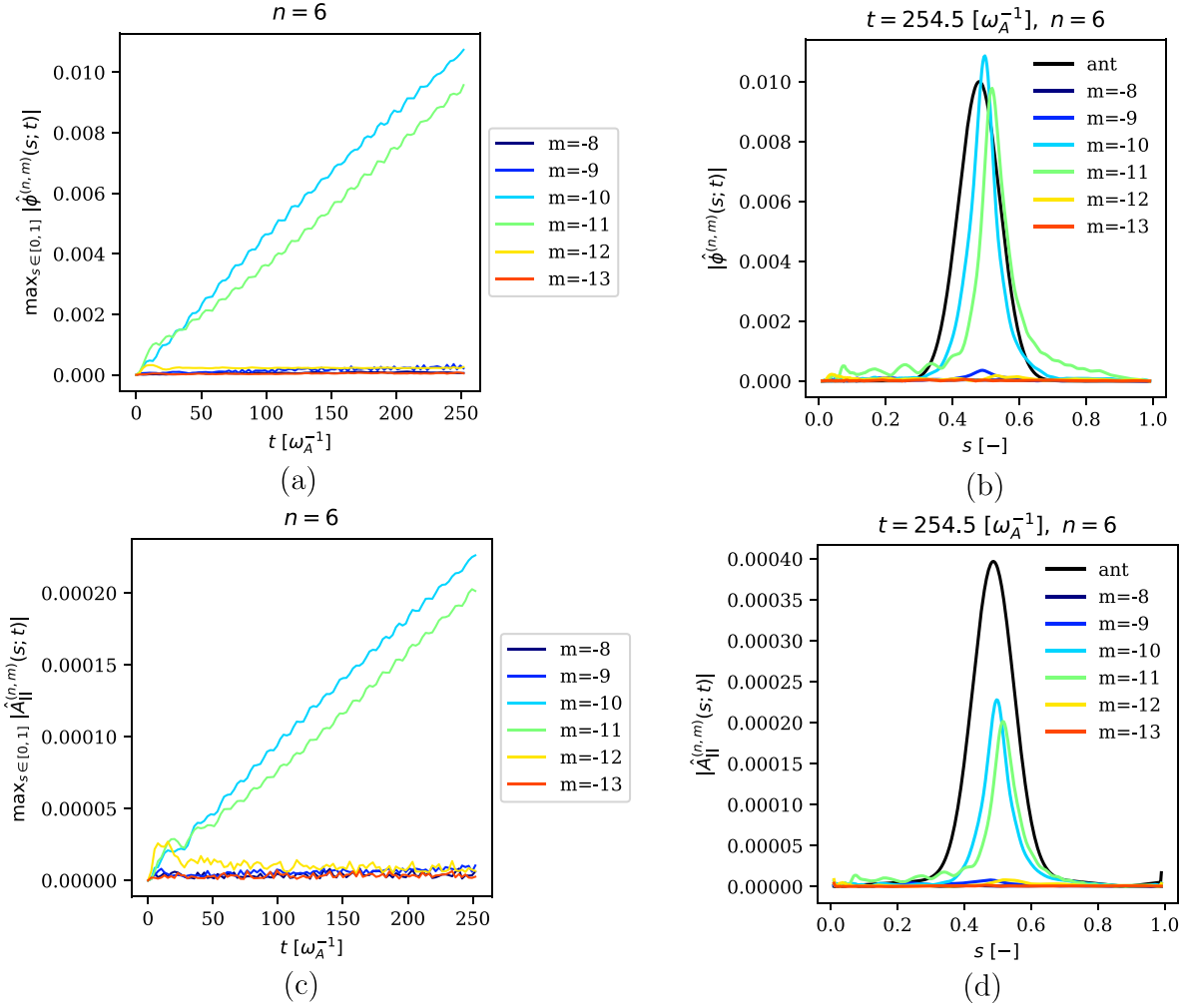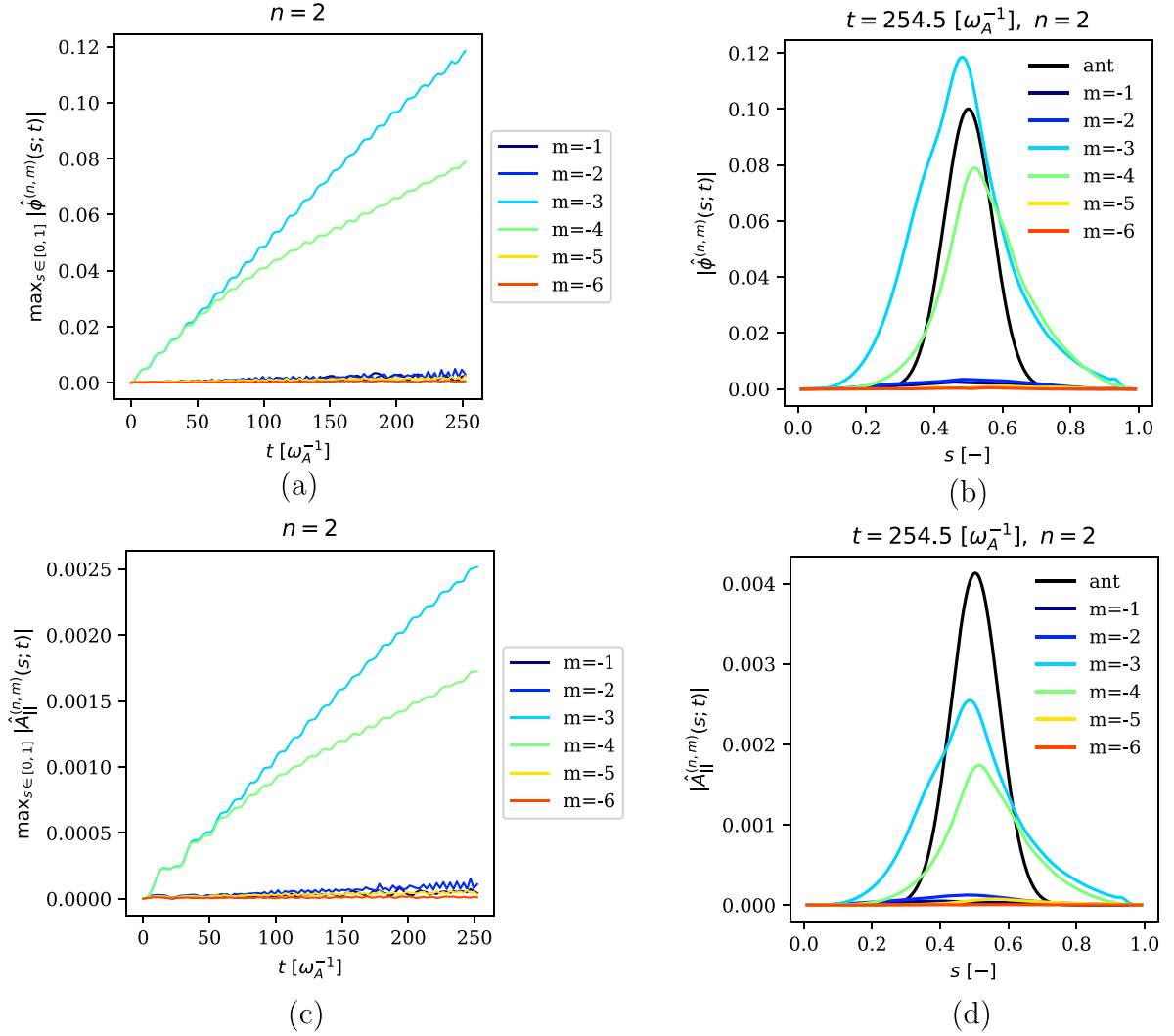
Figure 5. Evolution of discrete Fourier transform of (a) electrostatic and (c) electromagnetic plasma's potentials in maximum norm that is taken in the radial direction for the $n = 6$ TAE mode excitation with an electromagnetic antenna. The outcome radial profile of (b) electrostatic and (d) electromagnetic potentials are shown at final time $t = 50000\ \omega_{ci}^{-1} \approx 254.5\ \omega_A^{-1}$. The radial profile of antenna's potential for $n = 6$ and $m = -10$ is depicted in black for the comparison.

$N_e = 2 \times 10^7$ markers for electrons, $N_i = 10^7$ markers for ions, a grid of size $N_s \times N_\theta \times N_\phi = 320 \times 256 \times 128$, and a time step size of $\Delta t = 50\ \omega_{ci}^{-1}$. ORB5 uses the inverse of the ion-cyclotron frequency $\omega_{ci}^{-1} = q_i B_0/(m_i c)$ as the unit for time where c is the speed of light. However, here we show the simulation results in the inverse of Alfvén frequency ω_A^{-1} as the relevant unit for time where $\omega_A = v_{A0}/R_0$ with Alfvén velocity on the axis $v_{A0} = B_0/\sqrt{\mu_0\ \rho_0}$, background plasma mass density ρ_0 and magnetic field strength B_0 evaluated on the axis $s = 0$. Note the ratio $\omega_{ci}/\omega_A \approx 196.5$ for the ITPA test case. In the case of fast particles, $N_f = 2 \times 10^7$ markers are considered. Here, we have used ten times more particles in the nonlinear simulations compared to the linear ones. Furthermore, we impose a Fourier filter that only includes the poloidal modes within $|m + \lfloor nq \rfloor| < 5$ where $\lfloor . \rfloor$ indicates the nearest integer, and the Dirichlet boundary condition at the axis and in the edge for the potentials. The kinetic equation is solved within an annular of $s \in [0.01, 0.99]$.

4.2. Linear simulations

Here, we consider the electromagnetic antenna in the linear setting and excite TAE modes in order to study their damping rate and frequency. In particular, we consider the zeroth-order equations of motion equations (2) and (3) and the first-order electromagnetic antenna contribution within linear pullback scheme equations (38)–(40), while setting the plasma response to zero in the equations of motion, i.e. $\dot{\boldsymbol{R}}_{plasma}^{(1)\ lin.fields}$ and $\dot{v}_{plasma}^{(1)\ lin.fields}$ in the left hand side of kinetic equation (1). It is worth noting that in the absence of an antenna, guiding centers of the particles would only follow the unperturbed equilibrium background fields in the linear setting.

4.2.1. Excitation of TAE modes.
In order to excite the $n = 6$ TAE mode, let us consider the antenna with $\mathcal{T} = \{(n_1, m_1), \ldots\} = \{(6, -11), (6, -10)\}$, the frequency

Figure 6. Evolution of discrete Fourier transform of (a) electrostatic and (c) electromagnetic plasma's potentials in maximum norm that is taken in the radial direction for the $n = 2$ TAE mode excitation with an electromagnetic antenna. The outcome radial profile of (b) electrostatic and (d) electromagnetic potentials are shown at final time $t = 50\,000\ \omega_{ci}^{-1} \approx 254.5\ \omega_A^{-1}$. The radial profile of antenna's potential for $n = 2$ and $m = -3$ is depicted in black for the comparison.

$\omega_{ant} = -0.280995\ \omega_A = -0.00143\ \omega_{ci}$, and Gaussian radial profiles

$$h_i(s) = a_i \exp\left(-(s - s_{0,i})^2 / \delta_i^2\right) \quad \text{for } i = 1, 2 \quad (45)$$

where $a_1 = 0.01, \quad s_{0,1} = 0.48, \quad \delta_1 = 0.087,$ (46)

and $a_2 = 0.01, \quad s_{0,2} = 0.52, \quad \delta_2 = 0.082.$ (47)

Similarly, for the $n = 2$ TAE mode, we consider the antenna with $\mathcal{T} = \{(n_1, m_1), \ldots\} = \{(2, -4), (2, -3)\}$, the frequency $\omega_{ant} = -0.280995\ \omega_A = -0.00143\ \omega_{ci}$ and radial profile

$$h_i(s) = a_i \exp\left(-(s - s_{0,i})^2 / \delta_i^2\right) \quad \text{for } i = 1, 2 \quad (48)$$

where $a_1 = 0.1, \quad s_{0,1} = 0.5, \quad \delta_1 = 0.1,$ (49)

and $a_2 = 0.1, \quad s_{0,2} = 0.5, \quad \delta_2 = 0.1.$ (50)

In both cases, the antenna's electrostatic potential takes the form

$$\phi_{ant} = \text{Re}\left[\sum_{i=1}^{2} h_i(s) e^{\hat{i}(n\theta + m_i\phi)} e^{\hat{i}\omega_{ant}t}\right] \quad (51)$$

where $n = 6$, $m = -11, -10$ for the case targeting $n = 6$ TAE mode, and $n = 2$ and $m = -4, -3$ for the case targeting $n = 2$ TAE mode. The parameters of the Gaussian shape functions were found by fitting the function in the radial direction to the TAE excited simulations obtained with fast ion particles.
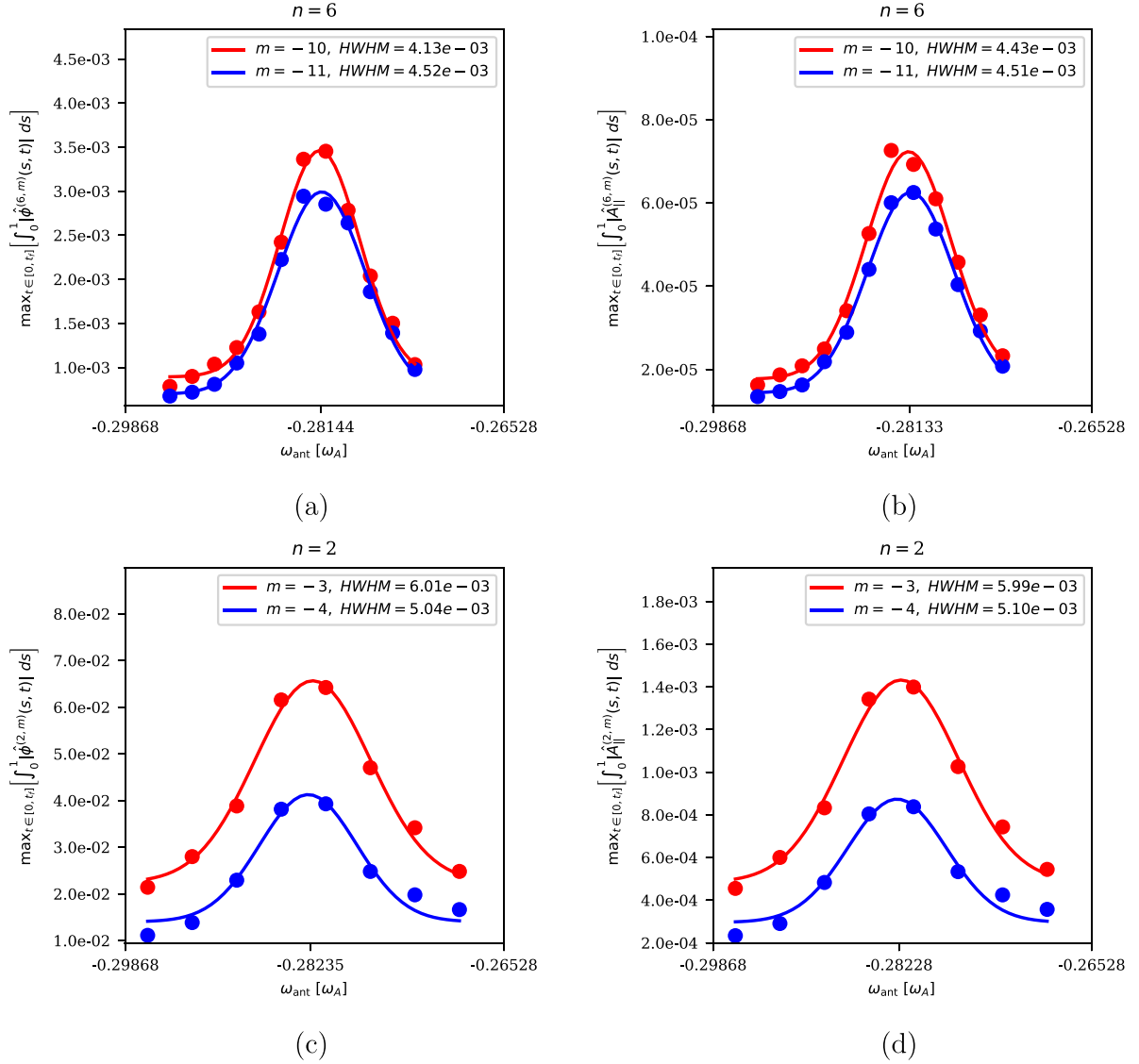
Figure 7. Linear excitation of the $n = 6$ (top) and the $n = 2$ (bottom) TAEs with an electromagnetic antenna at a range of frequencies near the resonance. Here, the amplitude of the plasma's potential is integrated in the radial direction and its maximum over a time span of $t \in [0, t_f]$ where $t_f = 200\,000\,\omega_{ci}^{-1} \approx 1017.8\,\omega_A^{-1}$ is taken (shown as points). The solid curves indicate the profiles of a Gaussian fit to the data points. The deployed antenna includes the mode $(n, m) \in \{(6, -10), (6, -11)\}$ for the excitation of the $n = 6$ TAE mode and $(n, m) \in \{(2, -4), (2, -3)\}$ for the excitation of the $n = 2$ TAE mode. This analysis is performed on the electrostatic ϕ (a)–(c) and electromagentic potentials $A_{||}$ (b)–(d).

Choosing such excitation parameters leads to the excitation of target modes in the plasma, as shown in figures 3 and 4 (only the plasma's response is presented here). The time traces and the radial profiles of the discrete Fourier transform of the electrostatic and magnetic potentials, shown in figures 5 and 6, indicate that the antenna has excited the target modes.

Furthermore, in order to find the resonance frequency numerically, simulations were repeated with the antenna at a range of frequencies, see figure 7. Since the maximum point of the potentials may oscillate in the radial direction over time, we consider

$$\int_0^1 |\hat{Q}|^{(n,m)}(s,t)\mathrm{d}s \tag{52}$$

as the measure where $|\hat{Q}|^{(n,m)}$ denotes the amplitude of the mode (n, m) for the potential of interest. By fitting a Gaussian function to the outcome set of points, we observe that the half-width-half-maximum (HWHM) of the $n = 6$ TAE mode is HWHM $\approx 2.2 \times 10^{-5}\omega_{ci}$ with the resonance frequency of $\omega_{res} \approx -0.001432\,\omega_{ci} \approx -0.2813\,\omega_A$. Similar measurements for the $n = 2$ TAE mode lead to HWHM $\approx 2.7 \times 10^{-5}\,\omega_{ci}$ and resonance frequency is $\omega_{res} \approx -0.001437\,\omega_{ci} \approx -0.2823\,\omega_A$.

Although TAE modes can also be excited similarly with the positive sign for the frequency, the excited mode with $\omega_{ant} > 0$ has a higher damping rate compared to the $\omega_{ant} < 0$, as discussed in the next section. Please note that the convention for the poloidal and toroidal used in ORB5 is such that a negative frequency means a propagation in the ion
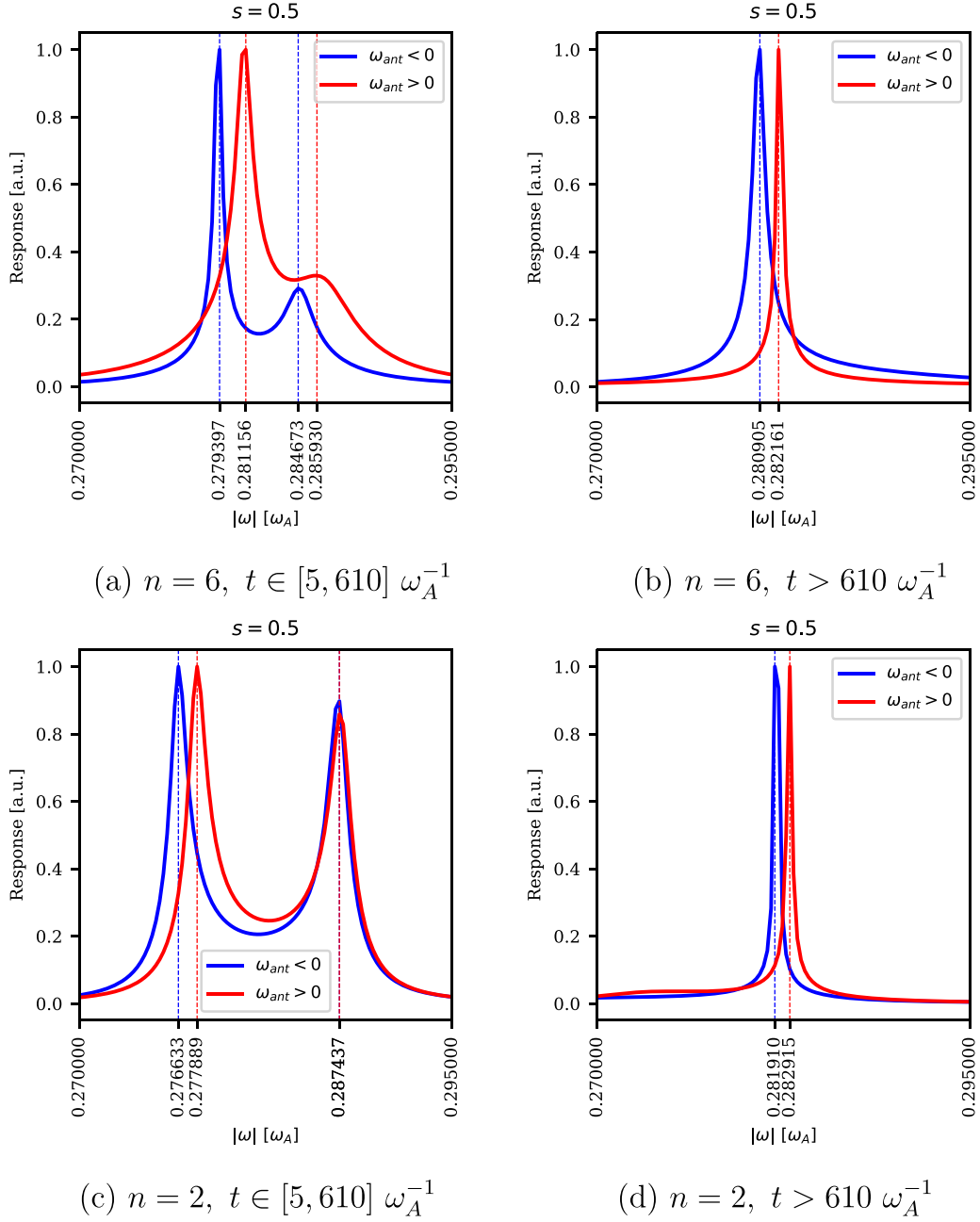
Figure 8. Frequency scan of the electrostatic potential of plasma at $s = 1/2$ for the antenna excitation of (a) and (b) the $n = 6$ TAE mode and (c) and (d) the $n = 2$ TAE mode. The DMUSIC was deployed to analyse the frequencies.

diamagnetic drift direction. Here, we compare the outcome frequency analysis of the electrostatic potential for the antenna excitation of the $n = 6$ and $n = 2$ TAE modes excited by the antenna with frequency $\omega_{ant} = \pm 0.280995\ \omega_A$ where simulations for positive and negative signs are done separately. In this study, we used damped multiple signal classification (DMUSIC) [10] for the frequency analysis. The frequency scan shown in figure 8 indicates a slight asymmetry in the sign of the frequency of the modes. The corresponding radial mode structures of these modes are shown in figure 9.

Although the positive and negative frequency modes are very similar to each other, the main difference lies in their amplitude due to the stronger excitation of negative frequency modes, which will be shown to have lower damping rates than positive frequency modes. Furthermore, we observe that the antenna excites more than one frequency within the gap, see figure 10. Nevertheless, the closest frequency to the one of the antenna (with less than 1% relative difference) becomes dominant as the system is driven with the antenna for a longer time.
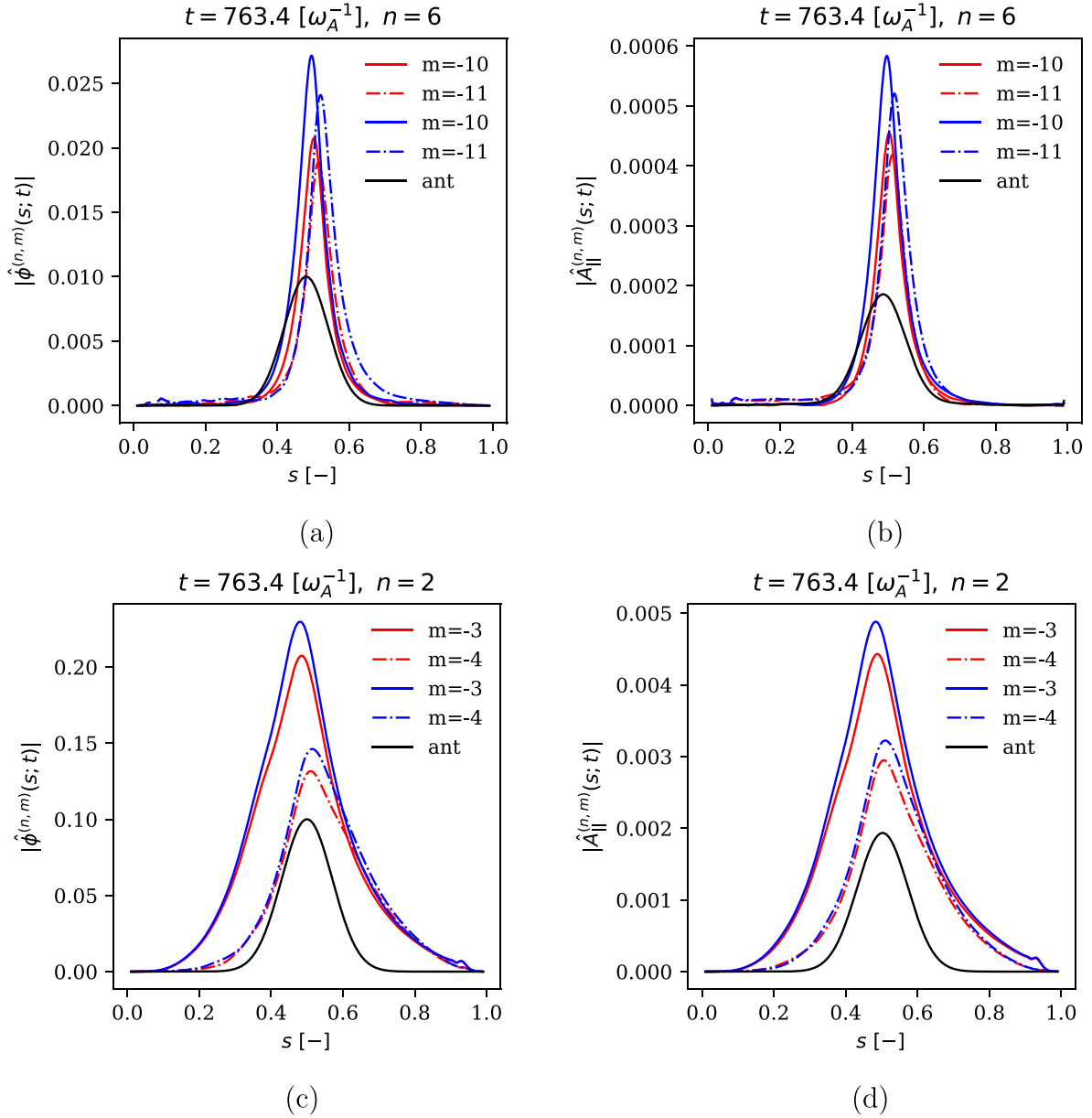
Figure 9. Radial profile of electrostatic and electromagentic potentials of plasma for the antenna excitation of (a) and (b) the $n = 6$ TAE mode and (c) and (d) the $n = 2$ TAE mode. Here, the blue and red colors correspond to excitation with $\omega_{ant} < 0$ and $\omega_{ant} > 0$, respectively. The radial profile of the antenna's potential for (a) and (b) $n = 6$ and $m = -10$, and (c) and (d) $n = 2$, $m = -3$ are plotted in black for the comparison.

4.2.2. Damping of TAE modes. After exciting the TAE mode with the antenna in linear simulations, we turn off the antenna and measure the damping rate as well as the dominant frequency of the system.

Considering a similar simulation setting to that in section 4.2.1, we deploy the electromagnetic antenna in the linear pullback scheme with the linear plasma response in two series of simulations; one with $\omega_{ant} = +0.00143\ \omega_{ci} = +0.280995\ \omega_A$ and the other with $\omega_{ant} = -0.00143\ \omega_{ci} = -0.280995\ \omega_A$, until $t = 50000\ \omega_{ci}^{-1} \approx 254.5\ \omega_A^{-1}$. Then, the simulations are continued without the antenna. As shown in figures 11 and 12 for the $n = 6$ and the $n = 2$ TAE modes, respectively, the potentials damp at a slightly faster rate with

$\omega_{ant} > 0$ compared to $\omega_{ant} < 0$, which has been previously in [9]. We recall that the TAE modes destabilized by fast ions have a negative frequency, which corresponds to modes propagating in the ion diamagnetic direction. Also, we note that our results are in agreement with the measured Landau damping results reported in [21] for electrons at a temperature of 1 keV.

Furthermore, we deployed the DMUSIC in order to numerically evaluate the frequency of the damped modes. As shown in figures 13 and 14, the dominant frequency of the system while the antenna is turned off is close to the target frequency, i.e. $\approx \pm 0.280995\ \omega_A$, which confirms further that the antenna has excited the mode of interest.
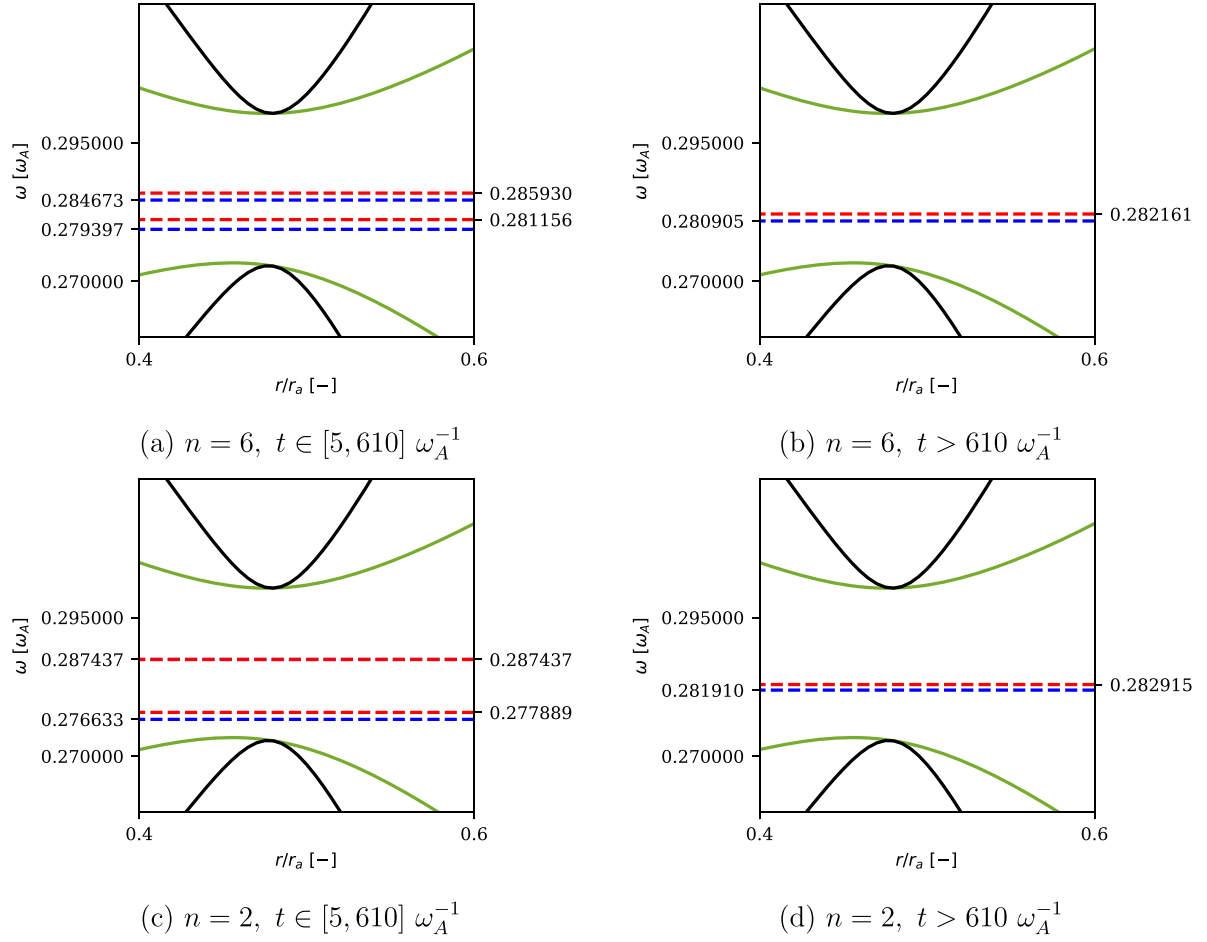
(a) $n = 6$, $t \in [5, 610] \ \omega_A^{-1}$

(b) $n = 6$, $t > 610 \ \omega_A^{-1}$

(c) $n = 2$, $t \in [5, 610] \ \omega_A^{-1}$

(d) $n = 2$, $t > 610 \ \omega_A^{-1}$

Figure 10. Peak of frequency scan for the electrostatic potential of plasma at $s = 1/2$ plotted in dashed lines (blue for $\omega_{\mathrm{ant}} < 0$ and red for $\omega_{\mathrm{ant}} > 0$) in the frequency spectra for the antenna excitation of (a) and (b) the $n = 6$ TAE mode and (c) and (d) the $n = 2$ TAE mode. The black solid curve corresponds to the Alfvén continua of $n = 6$, $m = -11, -10$ TAE mode and the green to $n = 2$, $m = -4, -3$ TAE mode of the ITPA test case, see figure 1.
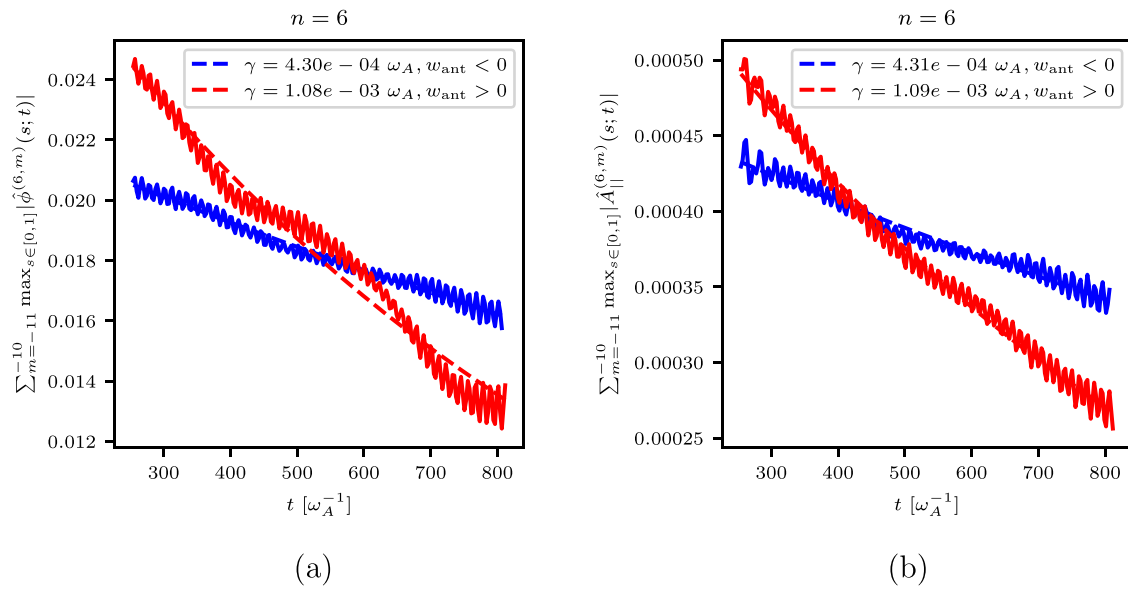
Figure 11. Damping rates of the $n = 6$ TAE mode obtained by fitting $ae^{-\gamma t}$ (dashed) to the corresponding Fourier coefficients of (a) ϕ and (b) $A_{||}$ of plasma integrated in the radial direction (solid curves). Here, the colors blue and red denote the simulation with $\omega_{\mathrm{ant}} = -0.280995 \ \omega_A$ and $\omega_{\mathrm{ant}} = 0.280995 \ \omega_A$, respectively.
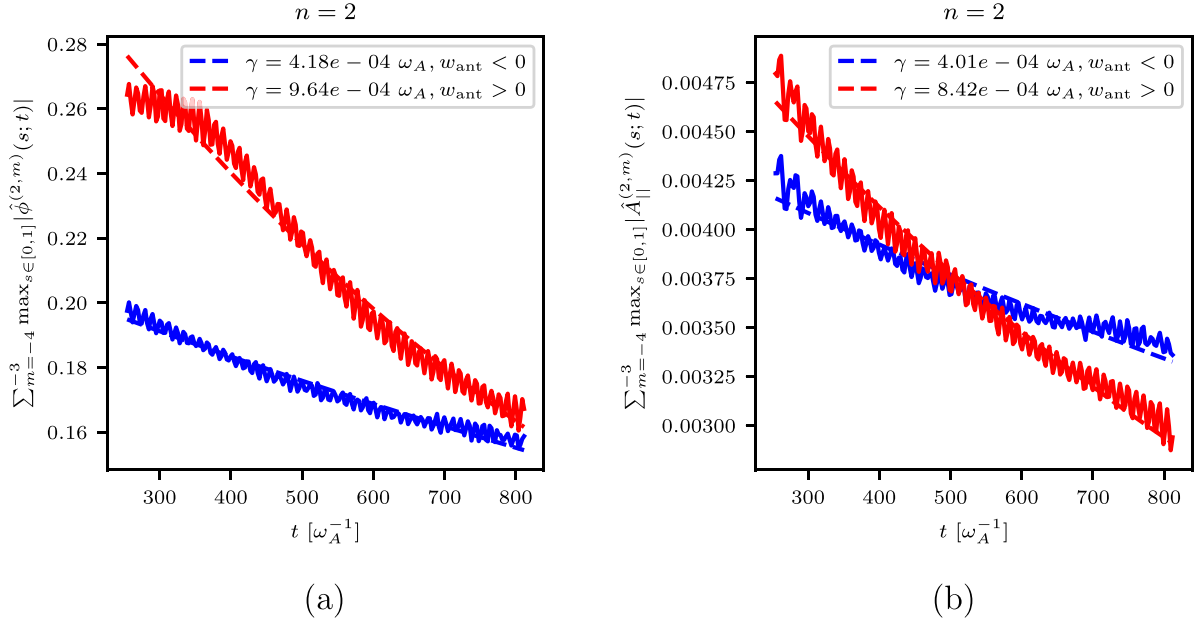
Figure 12. Damping rates of TAE modes, i.e. $(n,m) = (2,-4)$ and $(2,-3)$, obtained by fitting $ae^{-\gamma t}$ to the corresponding Fourier coefficients of (a) ϕ and (b) $A_{||}$ of plasma integrated in the radial direction. Here, the colors blue and red denote the simulation with $\omega_{\text{ant}} = -0.280995\,\omega_A$ and $\omega_{\text{ant}} = 0.280995\,\omega_A$, respectively.
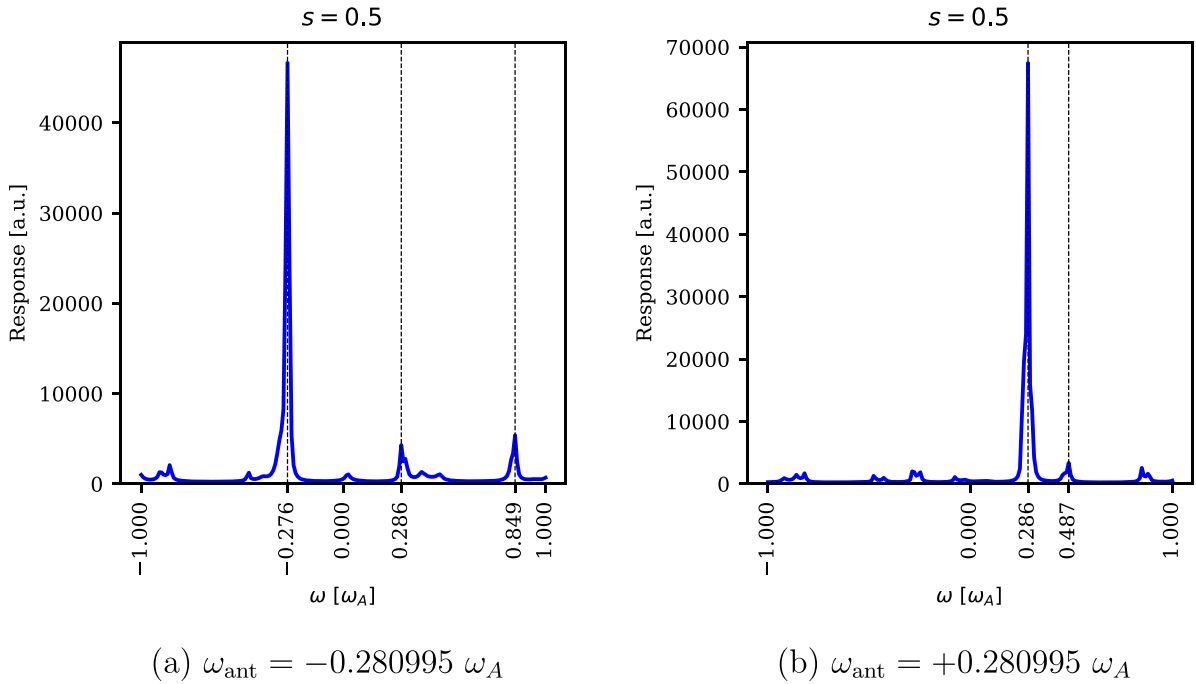

Figure 13. Frequency scan of ϕ at $s = 1/2$ for the damping $n = 6$ TAE mode for $t > 254.5\,\omega_A^{-1}$ using the DMUSIC method. The mode was initially excited by the antenna with the frequency (a) $\omega_{\text{ant}} = -0.280995\,\omega_A$ and (b) $\omega_{\text{ant}} = 0.280995\,\omega_A$ for $t < 254.5\,\omega_A^{-1}$.

4.2.3. Fast particle simulations using initial condition obtained by antenna. In this section, we study the growth rate of modes where fast particles are considered in the plasma. Instead of starting from an arbitrary initial condition, here we perform a preparation step where we excite the mode of interest using the antenna where the fast particles are included in the simulation with a negligibly small density fraction

$n_{0\text{f}} = 10^{-6}$. Once the mode is excited, i.e. $t = 50\,000\,\omega_{\text{ci}}^{-1} \approx 254.5\,\omega_A^{-1}$, we turn off the antenna and continue the simulation with the fast particles at a range of density. This test case is intended to confirm that the TAE mode is excited correctly with the antenna. Here, we target the $n = 6$ TAE mode.

As shown in figure 15, there is a clear exponential growth of the TAE mode for $t > 254.5\,\omega_A^{-1}$ as the antenna with
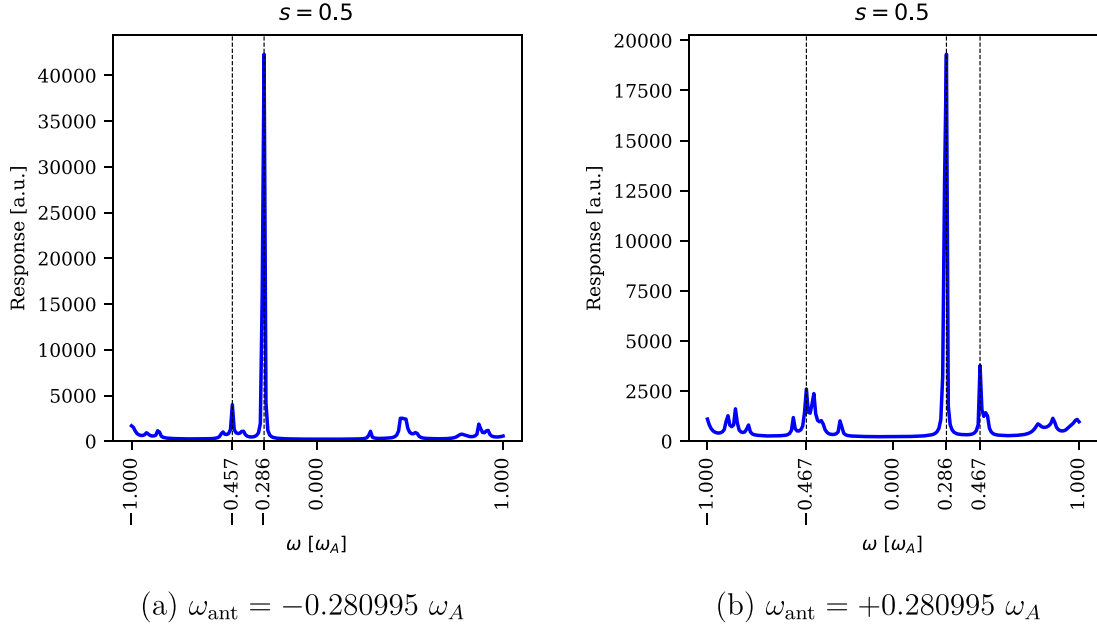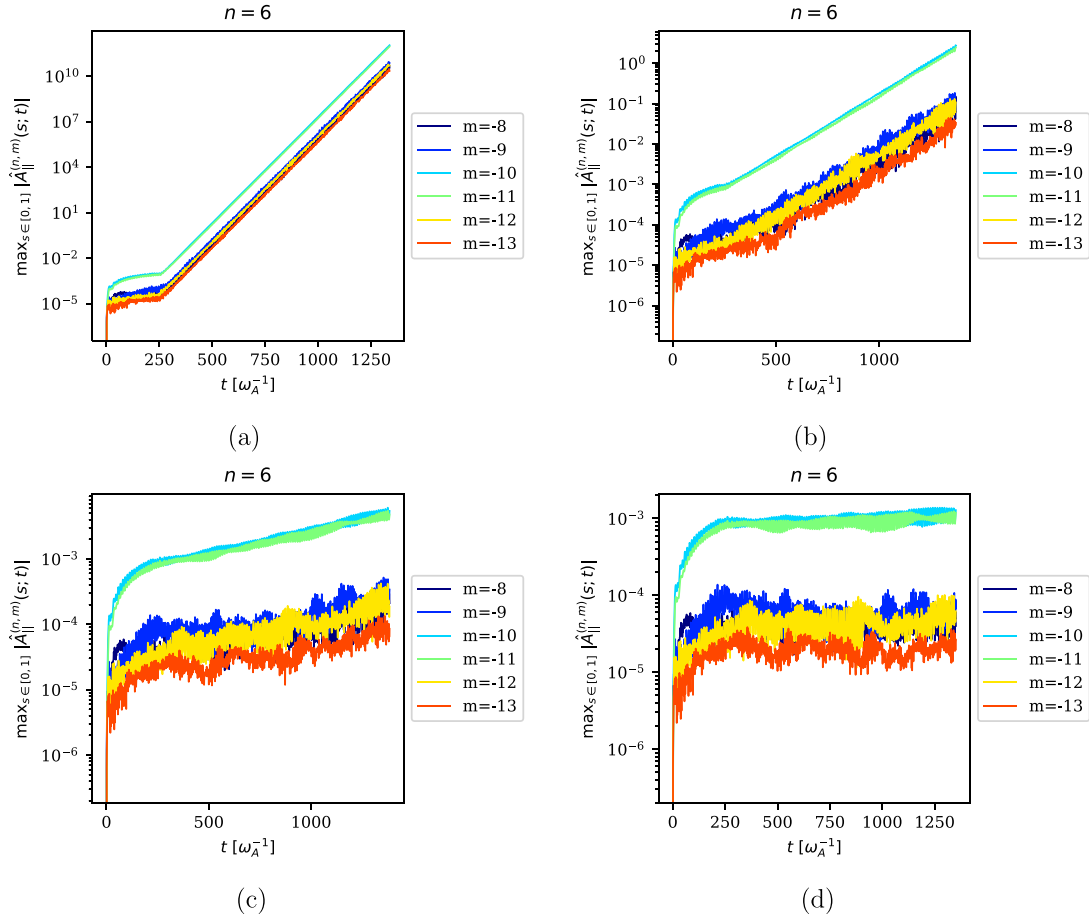
(a) $\omega_{\mathrm{ant}} = -0.280995\,\omega_A$

(b) $\omega_{\mathrm{ant}} = +0.280995\,\omega_A$

Figure 14. Frequency scan of ϕ at $s = 1/2$ for the damping $n = 2$ TAE mode for $t > 254.5\,\omega_{\mathrm{A}}^{-1}$ using DMUSIC method. The mode was initially excited by the antenna with the frequency (a) $\omega_{\mathrm{ant}} = -0.280995\,\omega_{\mathrm{A}}$ and (b) $\omega_{\mathrm{ant}} = 0.280995\,\omega_{\mathrm{A}}$ for $t < 254.5\,\omega_{\mathrm{A}}^{-1}$.

(a)

(b)

(c)

(d)

Figure 15. Evolution of Fourier coefficients $\left|\hat{A}_{||}^{(n,m)}\right|$ of plasma against time. The $n = 6$ TAE mode is excited in $t \in [0, 254.5]\,\omega_{\mathrm{A}}^{-1}$ using antenna with the frequency $\omega_{\mathrm{ant}} = -0.00143\,\omega_{\mathrm{ci}} = -0.280995\,\omega_{\mathrm{A}}$ while fast particles with a small density $n_{\mathrm{0f}} = 10^{-6}$ are incorporated in the simulation. Then, considering the resulting particle positions and velocities as the initial condition, the simulation is continued by increasing the density of fast particles to $n_{\mathrm{0f}} = n_0, n_0/4, n_0/16$ and $n_0/32$ where $n_0 = 0.0031$ in (a)–(d), respectively, for $t > 254.5\,\omega_{\mathrm{A}}^{-1}$.
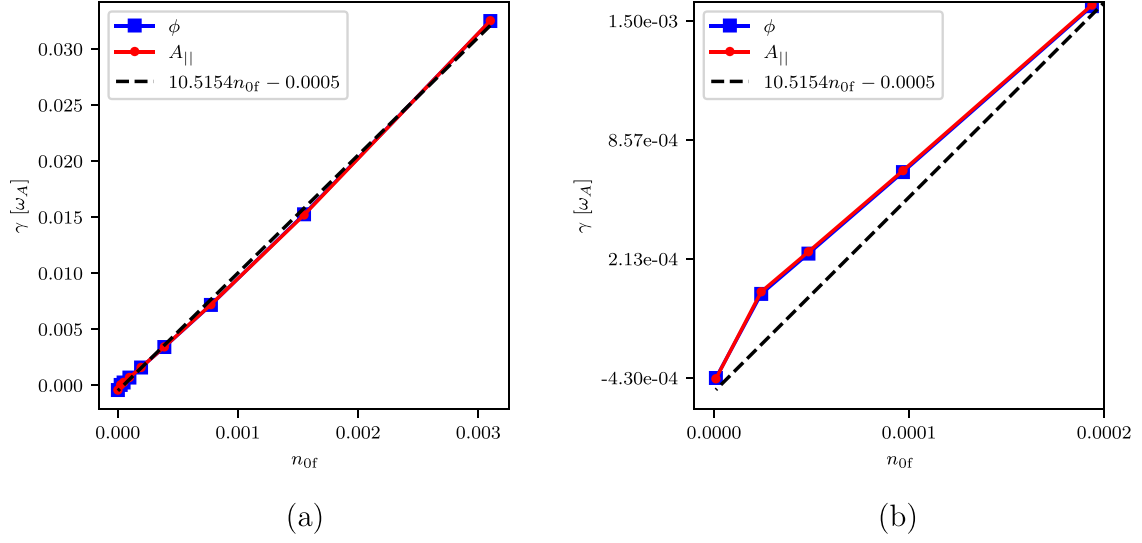
(a)

(b)

Figure 16. Growth rate γ of the $n = 6$ TAE mode against the normalized density fraction n_{0f} of fast particles is shown for (a) $n_{0f} < 0.004$ and (b) $n_{0f} < 0.0002$, where γ is obtained by fitting (dashed lines) $ae^{\gamma t}$ to the corresponding Fourier coefficients of ϕ and $A_{||}$ integrated in the radial direction for $t \in [500, 1000]\ \omega_A^{-1}$. Here, the $n = 6$ TAE mode is initially excited by the electromagnetic antenna with frequency $\omega_{ant} = -0.280995\ \omega_A$ for $t \in [0, 254.5]\ \omega_A^{-1}$.

(a)

(b)

(c)

(d)
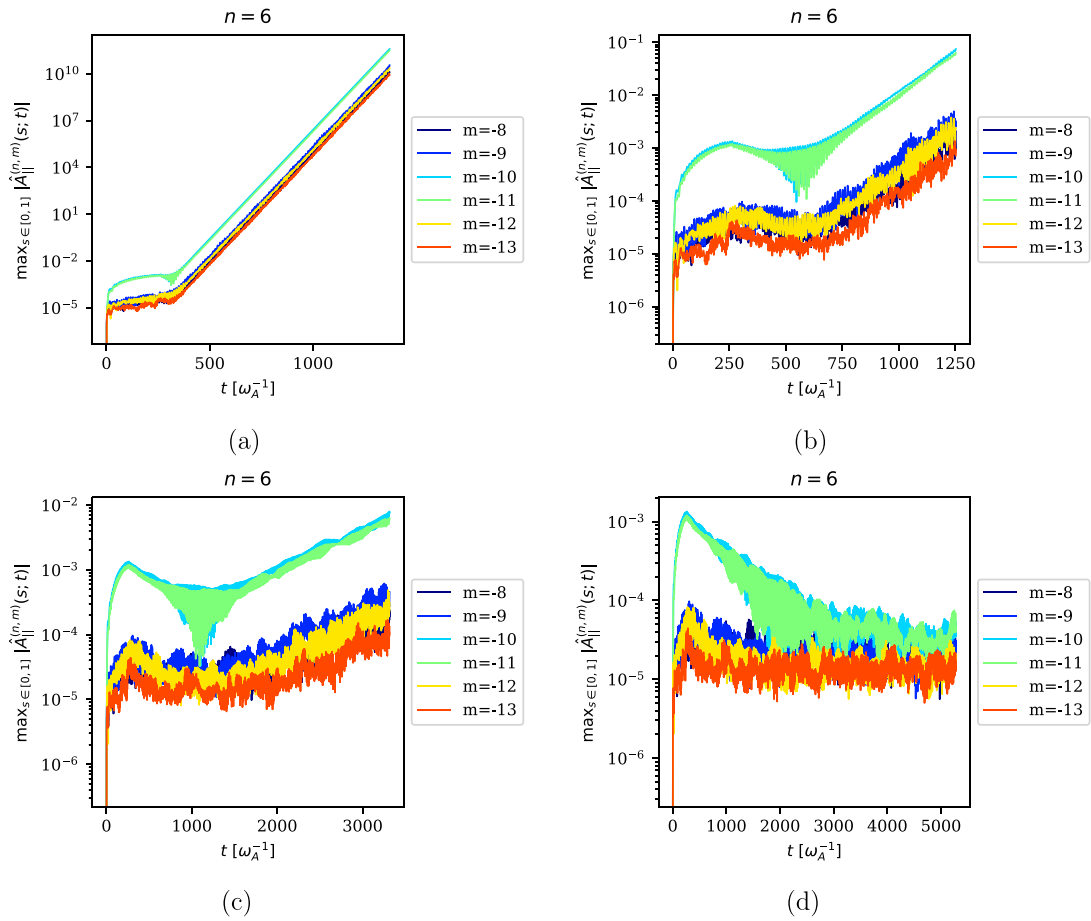
Figure 17. Evolution of Fourier coefficients $|\hat{A}_{||}^{(n,m)}|$ of plasma against time. The $n = 6$ TAE mode is excited in $t < 254.5\ \omega_A^{-1}$ using an antenna with the frequency $\omega_{ant} = +0.00143\ \omega_{ci} = +0.280995\ \omega_A$ while fast particles with a small density $n_{0f} = 10^{-6}$ are incorporated. Then, considering the resulting particle positions and velocities as the initial condition, the simulation is continued by increasing the density of fast particles to $n_f = n_0, n_0/4, n_0/16$ and $n_0/32$ where $n_0 = 0.0031$ in (a), (b), (c) and (d), respectively, for $t > 254.5\ \omega_A^{-1}$.
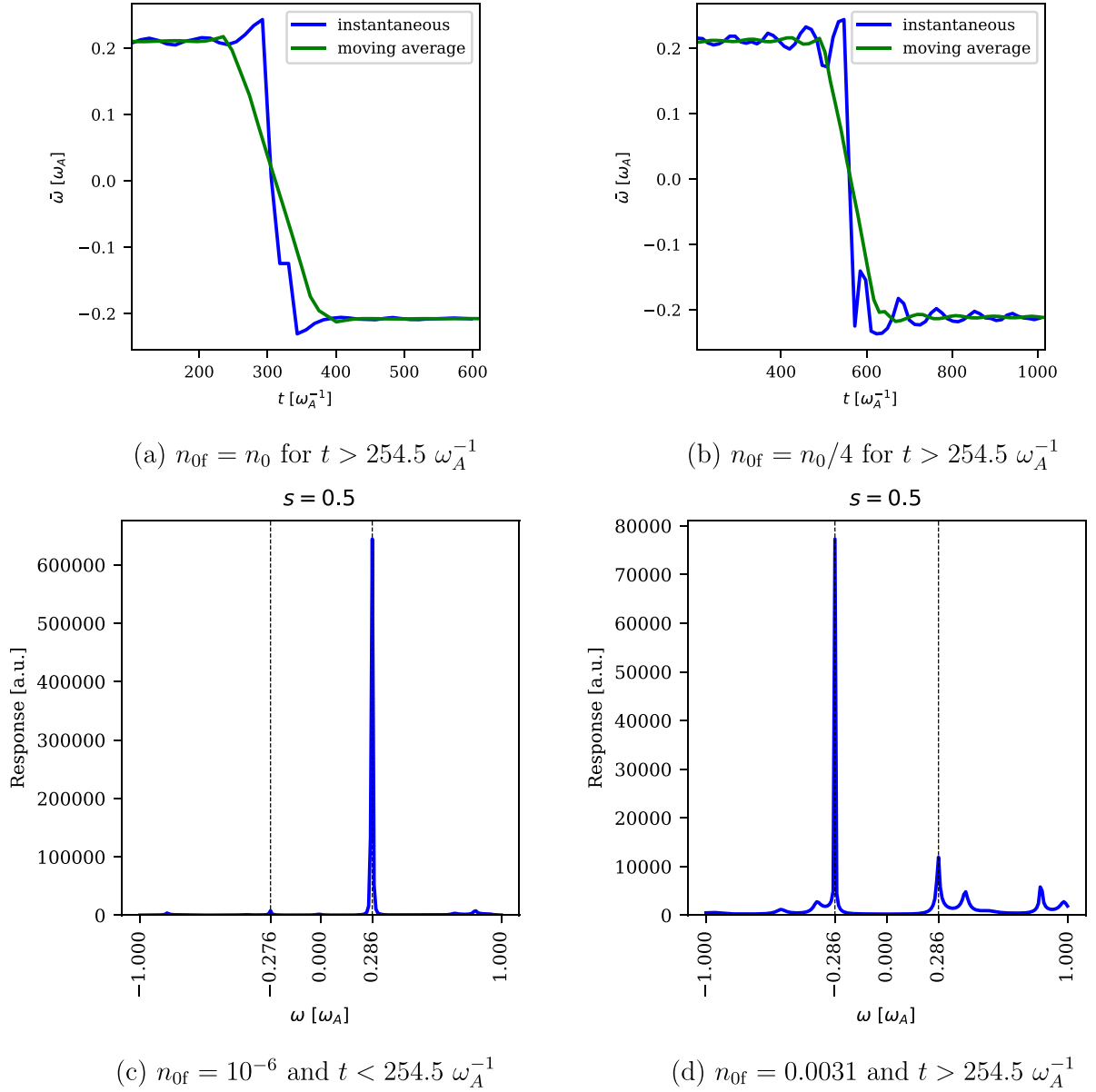
(a) $n_{0f} = n_0$ for $t > 254.5\,\omega_A^{-1}$

(b) $n_{0f} = n_0/4$ for $t > 254.5\,\omega_A^{-1}$

(c) $n_{0f} = 10^{-6}$ and $t < 254.5\,\omega_A^{-1}$

(d) $n_{0f} = 0.0031$ and $t > 254.5\,\omega_A^{-1}$

Figure 18. Change of direction in the mode propagation where excited $n = 6$ TAE mode with the frequency $\omega \approx +0.28\,\omega_A$ is overcome by the dominant mode with the frequency $\omega \approx -0.28\,\omega_A$. The frequency at which potentials propagate for the simulations of fast particles with density $n_{0f} = n_0$ and $n_{0f} = n_0/4$ with $n_0 = 0.0031$ are shown in (a) and (b), respectively. Here, the mode propagation frequency $\bar{\omega}$ of the field is computed instantaneously by computing the change in the phase of Fourier coefficient of ϕ at $s = 0.5$. The DMUSIC frequency scan of the potential of the case (a), shown in (c) before and (d) after injection of fast particles, shows a clear change of sign in the frequency.

$\omega_{ant} = -0.00143\,\omega_{ci} = -0.280995\,\omega_A < 0$ is turned off and fast particles are enabled in the simulation by considering number density fraction $n_{0f} > 10^{-6}$. The measured growth rate seems to be a linear function of fast particle number density, see figure 16.

Furthermore, we can investigate how the system evolves as $\omega_{ant} = 0.00143\,\omega_{ci} = 0.280995\,\omega_A > 0$ is used for excitation of the $n = 6$ TAE mode for $t < 254.5\,\omega_A^{-1}$. As smaller densities of fast particles are considered, the exponential growth of the TAE mode with the negative sign of frequency is postponed until it overcomes the damping rate of TAE mode with a positive sign of frequency from the antenna phase, see

figure 17. In fact, as the TAE mode with negative sign takes over, the direction of mode propagation reverses, see figure 18. Note that this transition of direction in the mode propagation becomes possible since at the time of switch off the amplitude of the unstable mode is nonzero, although small, see figure 18(c).

4.3. Nonlinear simulations

In this section, we deploy the antenna in order to excite TAE modes in the nonlinear setting, i.e. we solve the electromagnetic antenna adapted in the equations of motion (41)–(43)
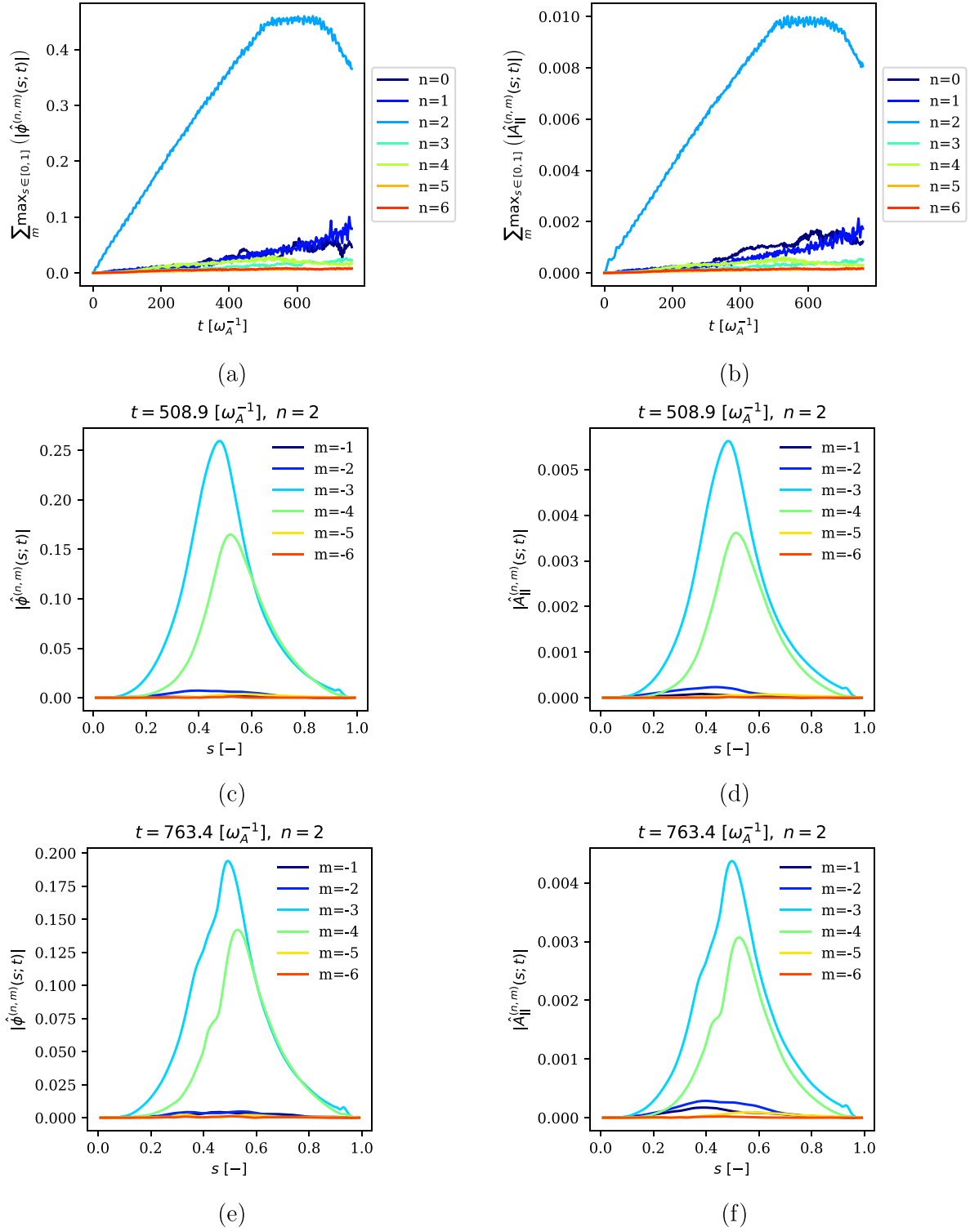
Figure 19. Nonlinear excitation of TAEs using the electromagnetic antenna with $n = 2$, $m = -3, -4$ and the frequency $\omega_{ant} = -0.280995\,\omega_A$. Here, time traces of ϕ and $A_{||}$ are shown in (a) and (b), respectively. The plasma's radial profiles of these modes at the time of turning off the antenna $t = 508.9\,\omega_A^{-1}$ (c)–(d) and after a period of relaxation at time $t = 763.4\,\omega_A^{-1}$ are shown in (e)–(f).
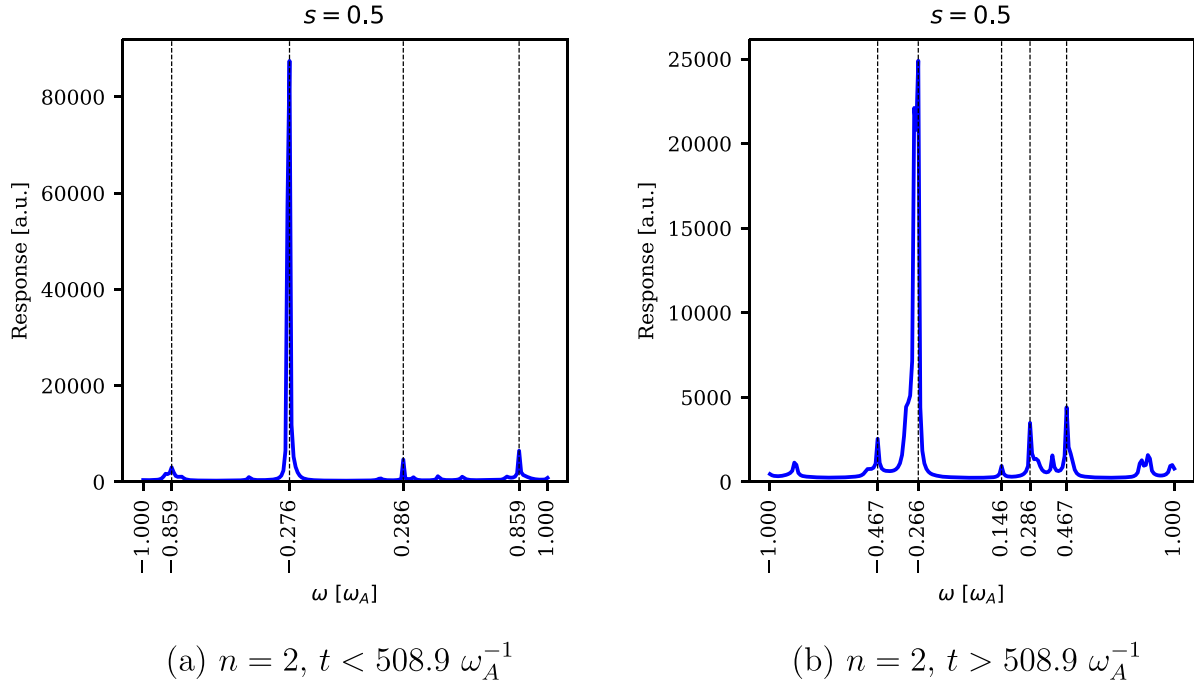
(a) $n = 2$, $t < 508.9\ \omega_A^{-1}$

(b) $n = 2$, $t > 508.9\ \omega_A^{-1}$

Figure 20. Frequency scan of ϕ for $n = 2$ toroidal mode number (a) during the antenna excitation $t < 508.9\ \omega_{\mathrm{A}}^{-1}$ and (b) during the damping phase with turned off antenna $t > 508.9\ \omega_{\mathrm{A}}^{-1}$ using DMUSIC for the nonlinear simulations where the $n = 2$ TAE mode is the target of the antenna.

which includes the zeroth and first-order plasma contribution equations (2) and (3) and equations (13)–(15) for the plasma. Here, the nonlinear pullback scheme equipped with the electromagnetic antenna where the ITPA case is taken as the test case. The parameters of the antenna are set similar to the linear simulations. Here, coupling among $n = 0, \ldots, 18$ toroidal mode numbers with poloidal mode numbers satisfying $|m + \lfloor nq \rfloor| \leqslant \Delta m$ where $\Delta m = 5$ was considered.

4.3.1. Excitation of the $n = 2$ TAE mode in a nonlinear simulation. In this section, we study nonlinear simulation of plasma in the ITPA test case equipped with the electromagnetic antenna to excite a TAE mode of interest. The antenna is set to target the $n = 2$ TAE mode with similar parameters as the one for the linear simulation, i.e. the description given in section 4.2.1. Here, we consider $\omega_{\mathrm{ant}} = -0.280995\ \omega_{\mathrm{A}}$ as the frequency of the antenna. The simulation has two phases. In the first phase, the $n = 2$ TAE mode is excited with the antenna till $t = 100000\ \omega_{\mathrm{ci}}^{-1} \approx 508.9\ \omega_{\mathrm{A}}^{-1}$. Then, the antenna is switched off for the damping phase of the mode.

As depicted in figure 19, the $n = 2$ TAE mode is excited clearly in the driving phase of the simulation, i.e. the $n = 2$ and $m = -3, -4$ are the dominant mode numbers at $s = 1/2$. However, during the damping phase, the mode structure in the radial direction is slightly disturbed. A frequency analysis of the mode for before and after switch off shown in figure 20 indicates that damping of the TAE mode allows other eigenfrequencies of the system to appear.

Here, we also investigate the plasma's nonlinear response if the antenna is deployed for a long time and never switched off. As shown in figures 21 and 22, by imposing the antenna that targets $n = 2$ TAE mode for a long time, other modes of the system, e.g. $(n, m) = (1, 0)$, are excited which is an example of mode-mode coupling that is driven with an antenna.

4.3.2. Excitation of TAE and GAE modes in a nonlinear simulation by an $n = 6$ TAE-like antenna. Although a clear excitation of the $n = 2$ TAE mode was obtained with the antenna in the nonlinear setting in section 4.3.1, the plasma response seems different in the case of exciting the $n = 6$ TAE mode. Here, we set the parameters of the antenna similar to section 4.2.1 and study the plasma response in $A_{||}$ and ϕ. The simulation has two steps. In the first part, the antenna is used to excite the desired mode and then, for $t > 100000\ \omega_{\mathrm{ci}}^{-1} \approx 508.9\ \omega_{\mathrm{A}}^{-1}$ the antenna is turned off.

As shown in figures 23–25, while the $n = 6$ TAE mode is excited as expected, several other modes appear to have been excited as well. Firstly, we observe that the interplay of modes has lead to the excitation of the $n = 2$ TAE mode along with toroidal mode numbers of $n = 0$ and $n = 1$. The frequency analysis of $n = 0$ (figure 25(c)) shows the nonlinear excitation of zonal structures, with frequencies very different from the antenna. The peaks at $\omega = \pm 0.578\ \omega_{\mathrm{A}}$ correspond to a $m = \pm 1$, $n = 0$ axisymmetric GAE. Those at $\omega = \pm 0.166\ \omega_{\mathrm{A}}$ are of unclear origin and deserve further investigations. The frequency analysis of $n = 1$ (figure 25(d)) also demonstrates the

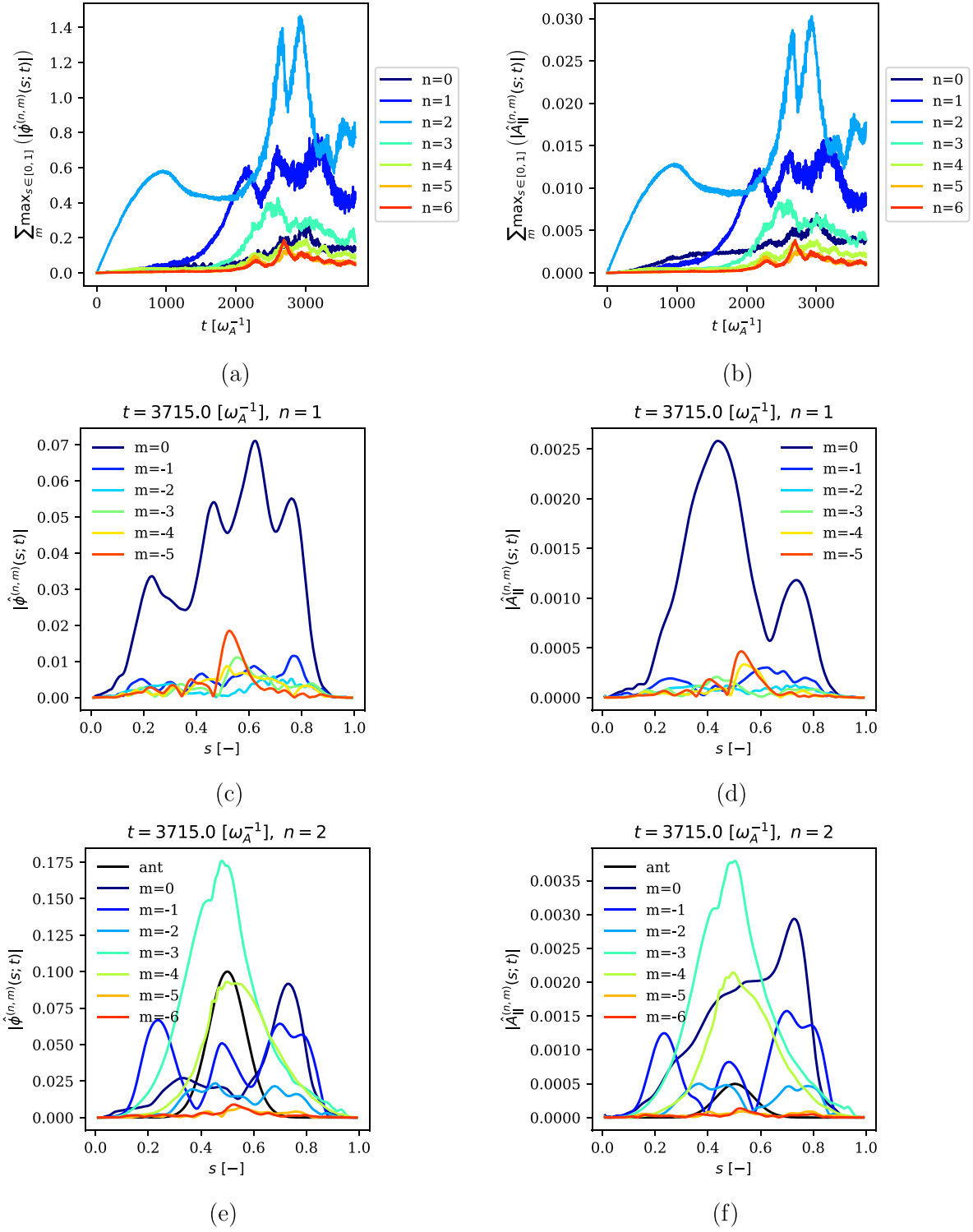**Figure 21.** Nonlinear excitation of TAEs using the electromagnetic antenna with $n = 2$, $m = -3, -4$ and the frequency $\omega_{ant} = -0.280995\,\omega_A$ which is deployed in the entire simulation. Here, time traces of ϕ and $A_{||}$ are shown in (a) and (b), respectively. The plasma's radial profiles of excited modes at the end of simulation $t = 3715\,\omega_A^{-1}$ for $n = 1$ (c)–(d) and $n = 2$ (e)–(f) are depicted.
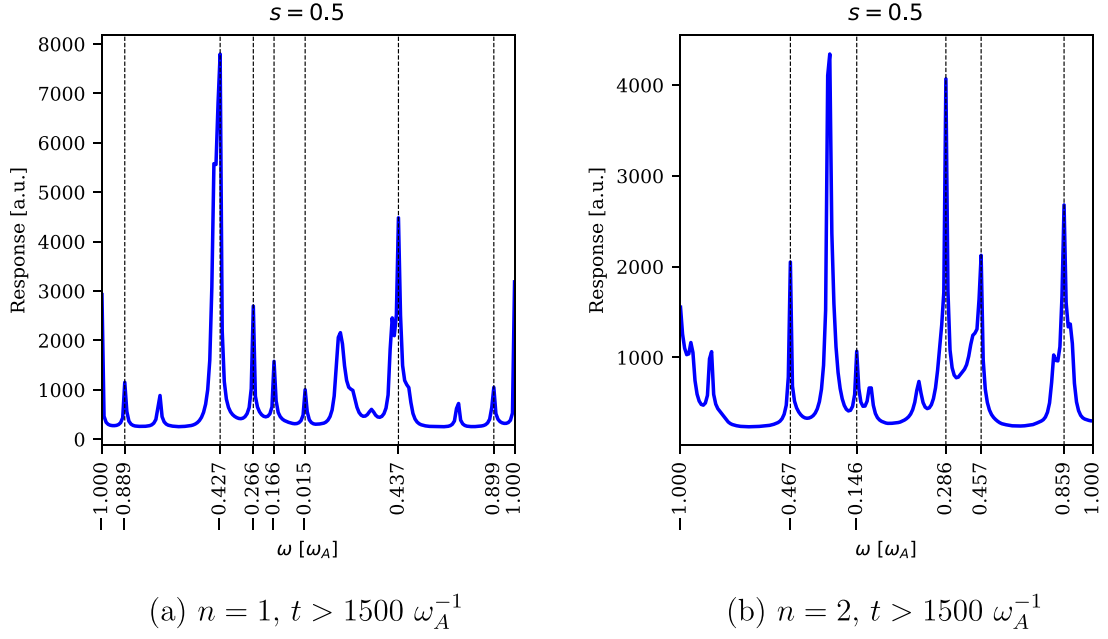
(a) $n = 1$, $t > 1500 \ \omega_A^{-1}$

(b) $n = 2$, $t > 1500 \ \omega_A^{-1}$

Figure 22. Frequency scan of ϕ for (a) $n = 1$ and (b) $n = 2$ toroidal mode numbers excited with the antenna that targets $n = 2$ TAE mode during entire nonlinear simulation. The frequency scan is carried out using DMUSIC.
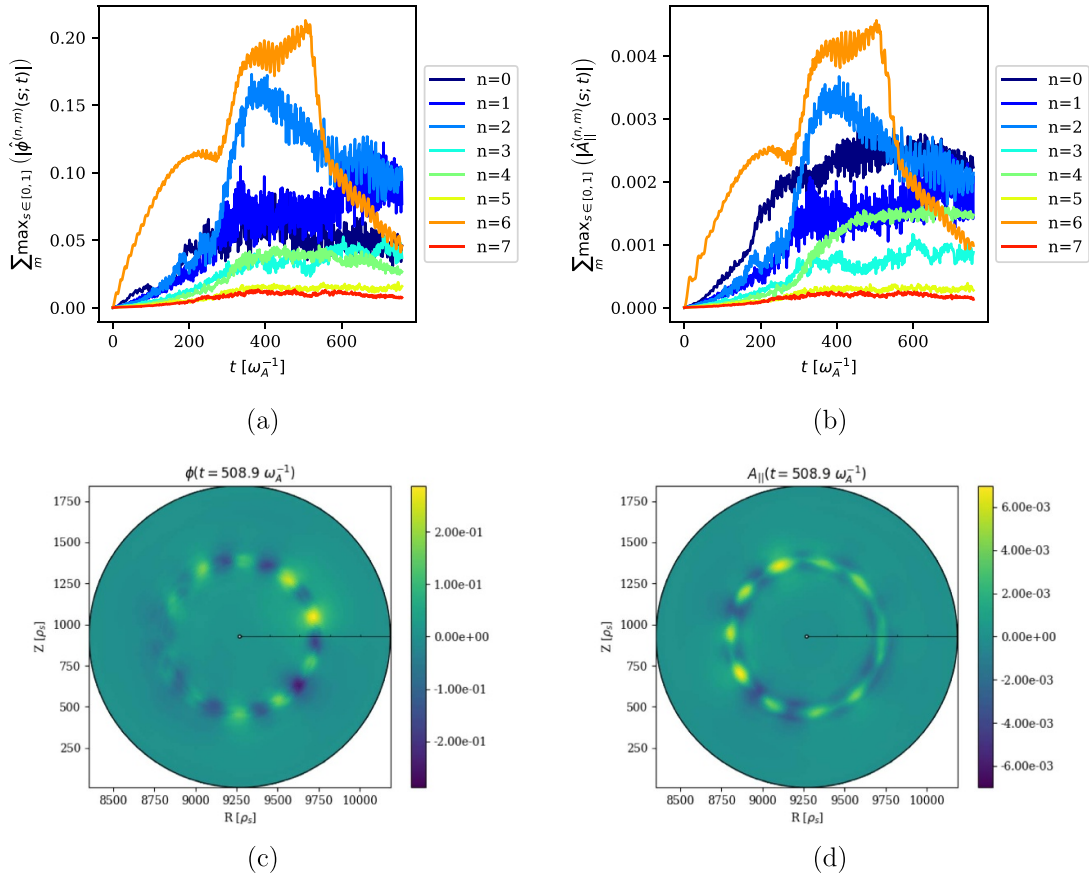
Figure 23. Evolution of plasma's (a) ϕ and (b) $A_{||}$ for the nonlinear simulation of the ITPA case with an antenna that is devised to excite the $n = 6$ TAE mode. The electrostatic and magnetic potentials at $t = 508.9 \ \omega_A^{-1}$ in the poloidal plane is depicted in (c) and (d), respectively.
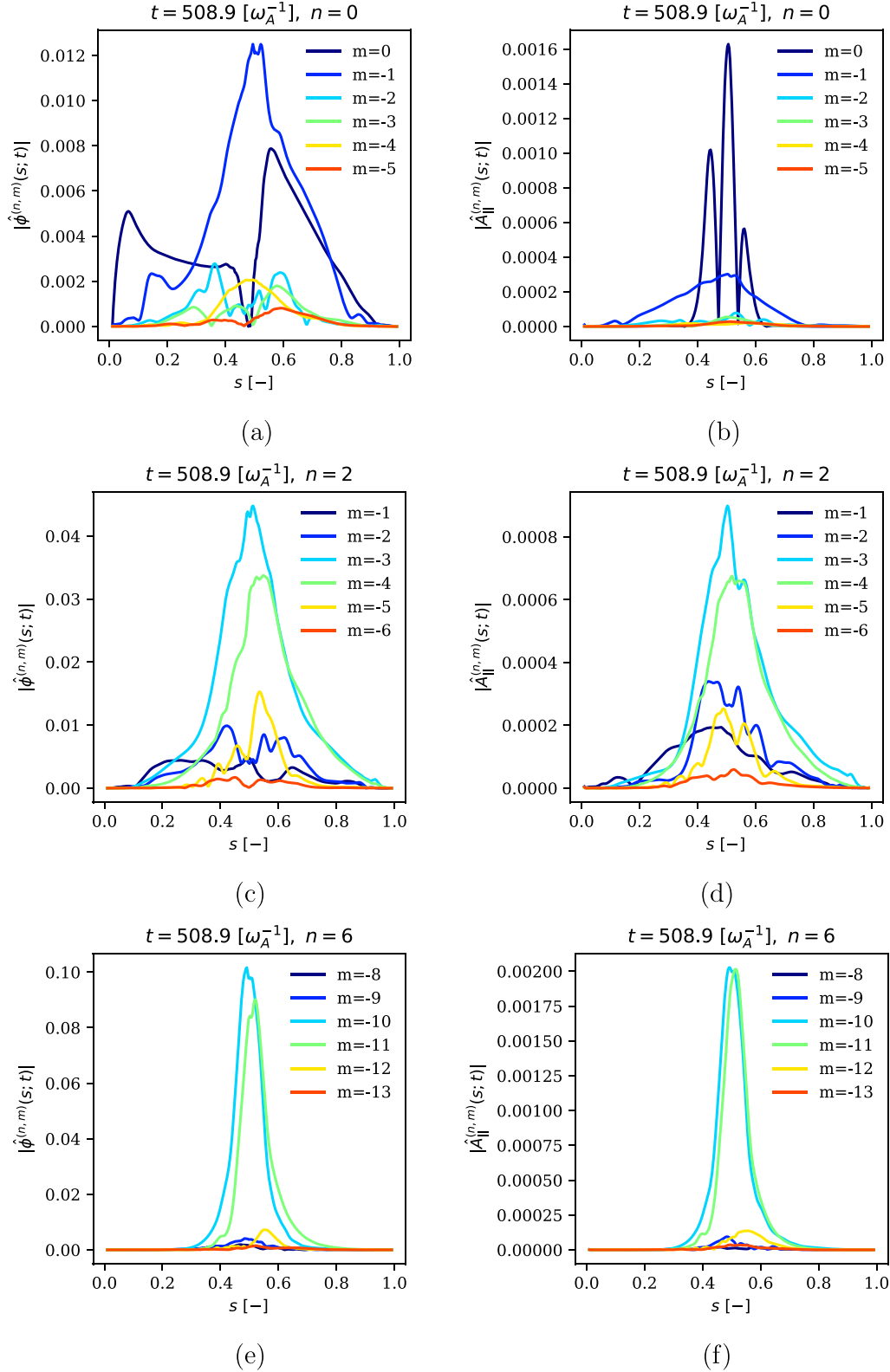
Figure 24. Radial profile of plasma's ϕ and $A_{||}$ at $t = 508.9\,\omega_A^{-1}$ for (a)–(b) $n = 0$, (c)–(d) $n = 2$ and (e)–(f) $n = 6$, respectively, obtained from nonlinear simulation where the $n = 6$ TAE mode is the target of the antenna.
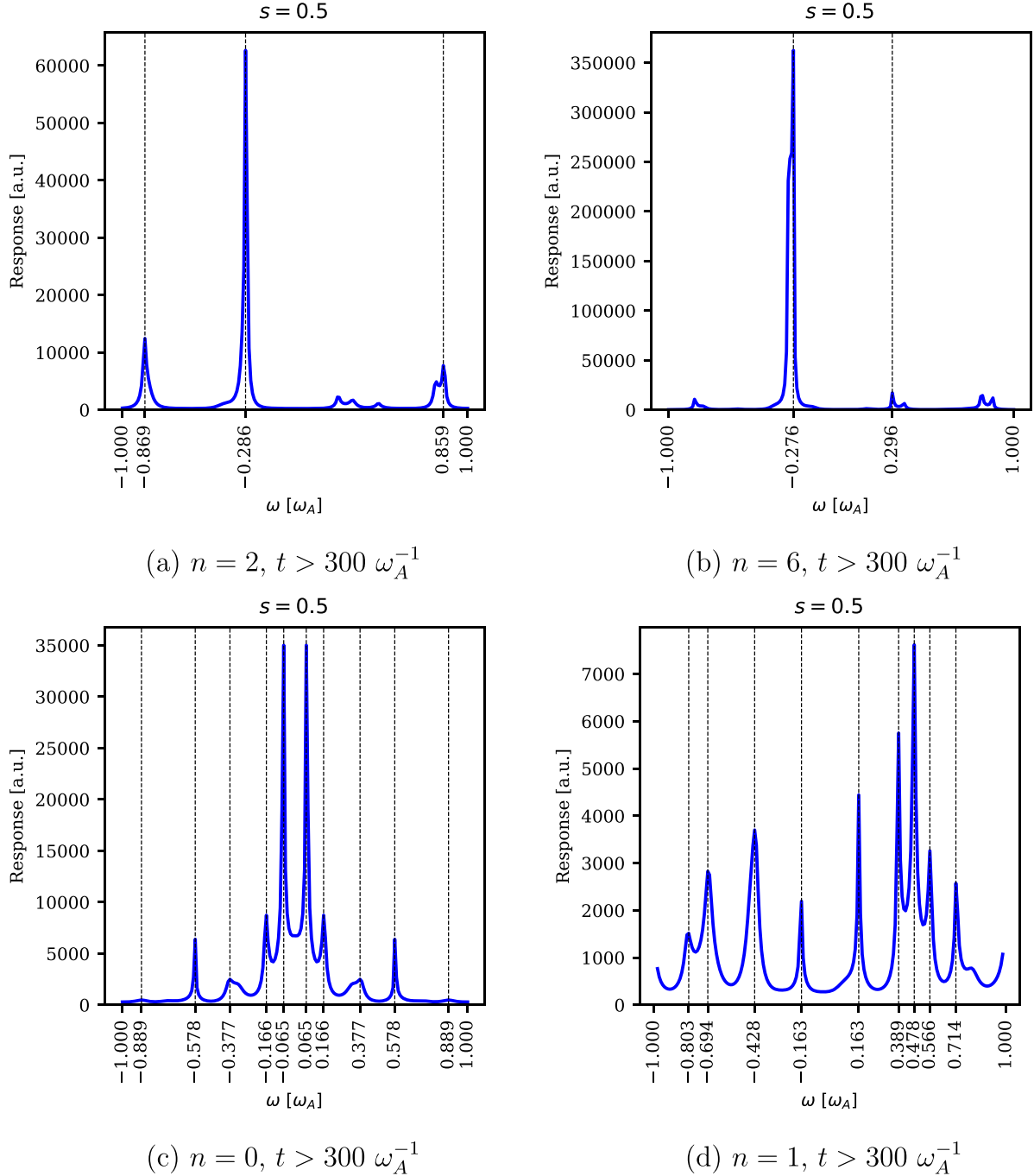
(a) $n = 2$, $t > 300 \, \omega_A^{-1}$

(b) $n = 6$, $t > 300 \, \omega_A^{-1}$

(c) $n = 0$, $t > 300 \, \omega_A^{-1}$

(d) $n = 1$, $t > 300 \, \omega_A^{-1}$

Figure 25. Frequency scan of ϕ for (a) $n = 2$, (b) $n = 6$, (c) $n = 0$, and (d) $n = 1$ toroidal mode numbers using DMUSIC for the nonlinear simulations where the $n = 6$ TAE mode is the target of the antenna.

nonlinear excitation of frequencies different from the antenna. The frequency peak at about $\omega = 0.4 \, \omega_A$ corresponds to a $m = -1, n = 1$ GAE.

5. Conclusion

In this study, we provide a detailed description of an antenna's implementation in ORB5 which allows an eigenmode of the system to be excited. First, the antenna is devised as an electrostatic potential, then the electromagnetic counterpart is computed using Ohm's law in order to deal with the cancellation problem. In order to obtain numerically stable simulations, the antenna's fields are integrated into the mixed-variable formulation and the pullback scheme. We deployed the antenna in linear and nonlinear simulations that aim to excite TAE modes. We have shown here that the frequency and the radial mode structure of the resulting excited mode is in good agreement with the one obtained from fast particle simulations. Furthermore, we show that it is possible to measure the damping rate of the TAE mode once the antenna is switched off. Although the target TAE mode can be excited in linear

simulations as expected, the antenna is shown to excite other modes in nonlinear simulations due to the coupling between the modes. In the example shown, an $n = 6$ TAE-like antenna is nonlinearly exciting an $n = 2$ TAE which has almost the same frequency as the antenna, but also $n = 0$ and $n = 1$ GAEs, at very different frequencies. Using forced external electromagnetic perturbations with the antenna setup is thus a useful tool to probe various nonlinear mode couplings.

Data availability statement

Acknowledgments

ORCID iDs

Mohsen Sadr https://orcid.org/0000-0003-0241-8163
Alexey Mishchenko https://orcid.org/0000-0003-1436-4502
Thomas Hayward-Schneider https://orcid.org/0000-0003-0588-5090
Alberto Bottino https://orcid.org/0000-0002-0514-8851
Alessandro Biancalani https://orcid.org/0000-0002-7227-6343
Peter Donnel https://orcid.org/0000-0002-6669-416X
Laurent Villard https://orcid.org/0000-0003-3807-9482

References

[1] Bass E and Waltz R 2010 Gyrokinetic simulations of mesoscale energetic particle-driven Alfvénic turbulent transport embedded in microturbulence *Phys. Plasmas* **17** 112319
[2] Biglari H, Zonca F and Chen L 1992 On resonant destabilization of toroidal Alfvén eigenmodes by circulating and trapped energetic ions/alpha particles in tokamaks *Phys. Fluids* B **4** 2385–8
[3] Briguglio S, Vlad G, Zonca F and Kar C 1995 Hybrid magnetohydrodynamic-gyrokinetic simulation of toroidal Alfvén modes *Phys. Plasmas* **2** 3711–23
[4] Brunner S, Fivaz M, Tran T and Vaclavik J 1998 Global approach to the spectral problem of microinstabilities in tokamak plasmas using a gyrokinetic model *Phys. Plasmas* **5** 3929–49
[5] Cheng C and Chance M 1986 Low-n shear Alfveén spectra in axisymmetric toroidal plasmas *Phys. Fluids* **29** 3695–701
[6] Cheng C Z 1991 Alpha particle destabilization of the toroidicity-induced Alfvén eigenmodes *Phys. Fluids* B **3** 2463–71
[7] Fasoli A, Borba D, Breizman B, Gormezano C, Heeter R, Juan A, Mantsinen M, Sharapov S and Testa D 2000 Fast particles-wave interaction in the Alfvén frequency range on the Joint European Torus tokamak *Phys. Plasmas* **7** 1816–24
[8] Fu G and Van Dam J 1989 Excitation of the toroidicity-induced shear Alfvén eigenmode by fusion alpha particles in an ignited tokamak *Phys. Fluids* B **1** 1949–52
[9] Kleiber R, Borchardt M, Könies A, Mishchenko A, Riemann J, Slaby C and Hatzky R 2018 Global gyrokinetic multi-model simulations of ITG and Alfvénic modes for tokamaks and the first operational phase of Wendelstein 7-X *27th IAEA Fusion Energy Conf. (Gandhinagar)*
[10] Kleiber R, Borchardt M, Könies A and Slaby C 2021 Modern methods of signal processing applied to gyrokinetic simulations *Plasma Phys. Control. Fusion* **63** 035017
[11] Könies A *et al* 2018 Benchmark of gyrokinetic, kinetic MHD and gyrofluid codes for the linear calculation of fast particle driven TAE dynamics *Nucl. Fusion* **58** 126027
[12] Lanti E *et al* 2020 ORB5: a global electromagnetic gyrokinetic code using the PIC approach in toroidal geometry *Comput. Phys. Commun.* **251** 107072
[13] Lauber P 2003 Linear gyrokinetic description of fast particle effects on the MHD stability in tokamaks *PhD Thesis* Technische Universität München
[14] Lauber P, Günter S, Könies A and Pinches S D 2007 LIGKA: a linear gyrokinetic code for the description of background kinetic and fast particle effects on the MHD stability in tokamaks *J. Comput. Phys.* **226** 447–65
[15] Lauber P, Günter S and Pinches S 2005 Kinetic properties of shear Alfvén eigenmodes in tokamak plasmas *Phys. Plasmas* **12** 122501
[16] Mishchenko A *et al* 2019 Pullback scheme implementation in ORB5 *Comput. Phys. Commun.* **238** 194–202
[17] Mishchenko A, Könies A, Kleiber R and Cole M 2014 Pullback transformation in gyrokinetic electromagnetic simulations *Phys. Plasmas* **21** 092110
[18] Nabais F *et al* 2018 TAE stability calculations compared to TAE antenna results in JET *Nucl. Fusion* **58** 082007
[19] Nishimura Y 2009 Excitation of low-n toroidicity induced Alfvén eigenmodes by energetic particles in global gyrokinetic tokamak plasmas *Phys. Plasmas* **16** 030702
[20] Ohana N T E 2020 Using an antenna as a tool for studying microturbulence and zonal structures in tokamaks with a global gyrokinetic GPU-enabled particle-in-cell code *PhD Thesis* EPFL, No.10127
[21] Vannini F, Biancalani A, Bottino A, Hayward-Schneider T, Lauber P, Mishchenko A, Novikau I and Poli E 2020 Gyrokinetic investigation of the damping channels of Alfvén modes in ASDEX Upgrade *Phys. Plasmas* **27** 042501
[22] Villard L, Brunner S and Vaclavik J 1995 Global marginal stability of TAEs in the presence of fast ions *Nucl. Fusion* **35** 1173
[23] Zhang W, Holod I, Lin Z and Xiao Y 2012 Global gyrokinetic particle simulation of toroidal Alfvén eigenmodes excited by antenna and fast ions *Phys. Plasmas* **19** 022507